

MUSEQuBES: The relation between Ly α emitters and C IV absorbers at $z \approx 3.3$

Eshita Banerjee ^{1*}, Sowgat Muzahid ¹, Joop Schaye ², Sean D. Johnson ³, and Sebastiano Cantalupo ⁴

¹ IUCAA, Post Bag 04, Ganeshkhind, Pune-411007, India

² Leiden Observatory, Leiden University, P.O. Box 9513, NL-2300 AA Leiden, the Netherlands

³ Department of Astronomy, University of Michigan, 1085 S. University, Ann Arbor, MI 48109, USA

⁴ Department of Physics, University of Milan Bicocca, Piazza della Scienza 3, I-20126 Milano, Italy

Accepted XXX. Received YYY; in original form ZZZ

ABSTRACT

We present a detailed study of the column density and covering fraction profiles of C IV absorption around 86 redshift $z \approx 3.3$ Ly α emitters (LAEs) detected in 8 Multi-Unit Spectroscopic Explorer (MUSE) fields of $1' \times 1'$ centered on 8 bright background quasars as part of the MUSEQuBES survey. Using Voigt profile fitting of all the C IV absorbers detected along these 8 sightlines, we generated a “blind” absorbers’ catalog consisting of 489 C IV absorption components. We cross-matched this blind C IV catalog with the MUSE-detected LAE catalog and found a significant enhancement of C IV components within $\approx \pm 400 \text{ km s}^{-1}$ of the systemic redshifts of the LAEs. Neither the C IV column density (N) nor the Doppler parameter (b) of individual C IV components shows any significant anti-correlation with impact parameter (ρ) of the LAEs in the 68 percentile range of $90 \leq \rho \leq 230$ physical kpc (pkpc). We find a covering fraction of $\approx 60\%$ for a threshold $N(\text{C IV})$ of $10^{12.5} \text{ cm}^{-2}$, which is roughly twice as high as in random regions. The C IV covering fraction remains constant at $\approx 50\%$ for impact parameters in the range $150\text{--}250 \text{ pkpc}$ ($\approx 3\text{--}6R_{200}$). Using the covering fraction profile, we constrained the LAE–C IV absorber two-point correlation function, and obtained $r_0 = 3.2 \text{ h}^{-1} \text{ comoving Mpc (cMpc)}$ and $\gamma = 1.2$ for a threshold $N(\text{C IV})$ of $10^{13.0} \text{ cm}^{-2}$. The C IV covering fraction is found to be enhanced for the LAEs that are part of a “pair/group” compared to the isolated ones.

Key words: galaxies: halos – galaxies: high-redshift – quasars: absorption lines – intergalactic medium

1 INTRODUCTION

Based on the current consensus, the inward and outward flows of baryons driven by accretion and galactic winds, known as the “cosmic baryon cycle”, dictate the formation and evolution of galaxies. The imprints of this baryon cycle can be found in the circumgalactic medium (CGM), the gaseous medium in the neighbourhood of galaxies which serves as the interface between the interstellar medium (ISM) and the intergalactic medium (IGM). The gas in the CGM is diffuse, metal enriched, multiphase, and kinematically complex (see Tumlinson et al. 2017, for a review). The gas and metal masses in the CGM are comparable to those in the galaxies and can potentially explain the “halo missing baryons” (McGaugh et al. 2010; Werk et al. 2014) and “missing metals” problems (Peeples et al. 2014). Therefore, probing the CGM of galaxies at different cosmic epochs, and in different environments is crucial.

Owing to its very low density ($n_{\text{H}} \sim 10^{-3} \text{ cm}^{-3}$), it is challenging to probe the CGM in emission, particularly at large galactocentric distances. However, there is a growing num-

ber of studies reporting extended emission out to a few tens of kpc from normal galaxies (e.g., Wisotzki et al. 2018; Zabl et al. 2021; Dutta et al. 2023a) and a few hundreds of kpc from active galaxies (e.g., Cantalupo et al. 2014; Borisova et al. 2016), mostly using strong resonant lines such as Ly α and Mg II (but see Johnson et al. 2022). Due to scattering, these resonant lines are not reliable tracers of gas kinematics. Moreover, the lack of multiple transitions restricts the ability to constrain the physical and chemical properties of the CGM. On the other hand, owing to the linear dependence of optical depth on density, absorption is a more sensitive tracer of the low-density gas than emission. The spectra of bright background sources, such as quasars, are generally used to probe the diffuse gas in the CGM (e.g., Chen et al. 1998; Adelberger et al. 2003; Turner et al. 2014). However, bright background galaxies can also be used for similar studies (e.g., Steidel et al. 2010; Péroux et al. 2018; Rubin et al. 2018).

Different ionic or atomic transitions seen in quasar spectra probe different phases of the absorbing gas. The neutral or low ionization transitions such as those from H I and Mg II trace the cool ($T \sim 10^4 \text{ K}$), relatively dense gas phase, whereas highly ionized transitions such as those from C IV and O VI can probe the low density photoionized and/or collision-

* E-mail: eshitaban18@iucaa.in

ally ionized warm-hot ($T \sim 10^5 - 10^6$ K) gas phase. However, at high redshift ($z > 2$), C IV absorbers are predominantly photoionized due to the higher intensity of the extragalactic UV background radiation and the relatively lower ionization potential (47.8 eV) (e.g., Schaye et al. 2003; Muzahid et al. 2012). The higher oscillator strengths of the C IV transitions and high cosmic abundance of carbon make it a useful tool to probe the CGM. Moreover, the rest-frame wavelengths of the C IV doublet ($\lambda\lambda 1548, 1550$) are suitable to identify them in the red part of the quasar's Ly α emission using the doublet matching technique.

At low redshifts ($z < 0.1$), the connection between C IV absorbers and galaxies is well-studied (see e.g., Chen et al. 2001; Borthakur et al. 2013; Bordoloi et al. 2014; Liang & Chen 2014; Schroetter et al. 2021). These studies suggest that, unlike H I, C IV is closely tied to galaxies with virtually no absorbers detected beyond the virial radius (R_{vir}). The COSMOS survey with 43 sub- L^* galaxies with stellar masses $M_* \sim 10^9 M_\odot$ concluded that the CGM of low-mass galaxies contains more carbon within $\approx 0.5 R_{\text{vir}}$ than that present in the stars of those galaxies (Bordoloi et al. 2014). They also found that for star-forming galaxies the C IV covering fraction at a threshold equivalent width of 100 mÅ is $f_c = 60 - 80\%$ within $\approx 0.5 R_{\text{vir}}$. Burchett et al. (2016) obtained a C IV covering fraction of $\approx 33\%$ within the R_{vir} for galaxies of redshift $0.0015 < z < 0.015$. They found that the high-mass galaxies ($> 10^{9.5} M_\odot$) show an environmental dependence in which the galaxies with fewer companions have a larger C IV covering fraction. They claimed that when galaxy number density increases C V becomes the dominant ionization state, leading to lower covering fractions for C IV. The low-mass galaxies in their sample ($< 10^{9.5} M_\odot$) rarely exhibit C IV absorption ($f_c \approx 9\%$). Johnson et al. (2017) found for a sample of 18 star-forming dwarf galaxies of stellar mass $\sim 10^8 - 10^9 M_\odot$ at $z \approx 0.2$ that O VI is considerably more common than C IV within $\approx 3 R_{\text{vir}}$ of the low-mass galaxies.

CGM studies at high z are more limited because it is challenging to find galaxies at higher redshifts. The Keck Baryonic Structure Survey (KBSS) is the first major CGM survey at $2 < z < 3$ that probed the radial distribution and kinematics of gas (H I) and metals (e.g., C IV O VI) around galaxies (e.g., Adelberger et al. 2003; Adelberger et al. 2005; Steidel et al. 2010; Rakic et al. 2012; Turner et al. 2014; Rudie et al. 2012, 2019). A strong correlation between H I and C IV absorbers and Lyman Break Galaxies (LBGs) is observed in the KBSS (Adelberger et al. 2003; Adelberger et al. 2005; Turner et al. 2014). Steidel et al. (2010), for the first time, observed the CGM of star-forming LBGs using background galaxy spectra and measured the distributions of various metals (e.g., C IV Si II, and Si IV) within an impact parameter of ≈ 125 pkpc. They also showed the presence of broad P-Cygni profiles in higher ionization transitions which suggested strong outflows caused by the stellar winds from massive stars. Turner et al. (2014) with their $z \approx 2.4$ star-forming KBSS galaxies showed that C IV absorption is extended up to 2 pMpc in the transverse direction. Using Voigt profile fitting of various metal lines around 8 KBSS galaxies for which the quasar sightlines probe the regions within R_{vir} , Rudie et al. (2019) confirmed the multiphase nature of the CGM at high redshifts. They measured a covering fraction of $\approx 90\%$ for C IV within R_{vir} for a threshold column density of $10^{12.5} \text{ cm}^{-2}$.

None of these high z studies have investigated the connections between galaxy properties (e.g., SFR, environment) and CGM properties. Additionally, because of the narrow/broad-band color selections, KBSS galaxies are biased towards high stellar masses ($M_* \sim 10^{10} - 10^{11} M_\odot$) and high star-formation rates (SFRs $\gtrsim 10 M_\odot \text{ yr}^{-1}$). Since low-mass galaxies at high redshifts are too faint to be detected in continuum emission, CGM investigations at high redshifts have hitherto been limited to such massive, bright galaxies.

With the availability of state-of-the-art integral field spectrographs (IFS) such as VLT/MUSE (Bacon et al. 2010) and Keck/KCWI (Morrissey et al. 2018), it is now possible to detect high-redshift galaxies purely via emission lines (primarily via the Ly α emission) that are too faint to be detected in continuum emission. The MUSE Quasar-field Blind Emitters Survey (MUSEQuBES) is the first survey focused on studying the CGM around high- z ($3 < z < 4$), low-mass ($M_* \sim 10^9 M_\odot$), mildly star-forming (SFR $\sim 1 M_\odot \text{ yr}^{-1}$) Ly α emitters (LAEs) using background quasars (see Muzahid et al. 2020, 2021). The MUSEQuBES survey presented a sample of 96 LAEs, detected around 8 high- z , UV-bright ($V < 19$) quasars within the $1' \times 1'$ field of view (FOV) of MUSE. Using spectral stacking analysis, Muzahid et al. (2021) reported significant excess H I and C IV absorption near LAEs out to ≈ 250 pkpc in the transverse and $\pm 500 \text{ km s}^{-1}$ along the line of sight directions. Moreover, the H I and C IV equivalent widths were measured to be larger around pair/group LAEs than near isolated ones. A strong correlation between H I absorption and the SFR of the LAEs was also seen, which was not present for C IV. The recent MUSE Analysis of Gas around Galaxies (MAGG) survey also found a higher H I covering fraction near pair/group LAEs than around isolated LAEs (Lofthouse et al. 2023). They searched for LAEs around known strong H I absorbers ($\log_{10} N(\text{H I})/\text{cm}^{-2} > 16.5$) and confirmed that high column density absorbers and LAEs basically trace each other. Using the MAGG sample, Galbiati et al. (2023) reported the C IV covering fraction of $\approx 40\%$ out to ≈ 250 pkpc for a threshold of equivalent width of 0.1 \AA . The C IV covering fraction in 'group' is found to be ≈ 3 times higher compared to isolated LAEs. They further showed that the luminosity function of the LAEs associated with C IV absorbers having a factor of ≈ 2.5 higher normalization factor compared to the field LAEs.

Here we continue with the analysis of the MUSEQuBES data. We blindly searched for the C IV doublet along the 8 MUSEQuBES quasars and created a "blind" C IV catalog using Voigt profile decomposition of all the blindly detected C IV absorbers. We cross-matched this catalog with the MUSE-detected LAE catalog to explore possible relations between the C IV absorbers and LAEs at $z \approx 3.3$. In order to correct for the resonant scattering effects of the "Ly α redshifts"¹ we adopted the empirical relation obtained for the MUSEQuBES galaxies in Muzahid et al. (2020). The LAE redshifts lie between $2.9 - 3.8$, near the peak of the cosmic star formation rate density (Madau & Dickinson 2014). The lower bound on the redshift is set by the minimum wavelength covered

¹ The redshift determined from the peak of the Ly α emission line is often redshifted with respect to the systemic redshift owing to the resonant scattering of Ly α photons (e.g., Verhamme et al. 2006; Steidel et al. 2010).

Table 1. Summary of the quasar fields surveyed in this work.

Quasar ¹	RA _{qso} ²	Dec _{qso} ³	z_{qso} ⁴	N_{gal}^5	Median SNR ⁶	Limiting $N(\text{C IV})^7$	z_{min}^8	z_{max}^9
BRI1108-07	11:11:13.6	−08:04:02	3.922	22(17)	25	12.18	2.9	3.872
J0124+0044	01:24:03.0	+00:44:32	3.834	4(3)	72	11.72	2.9	3.786
PKS1937-101	19:39:57.3	−10:02:41	3.787	2(1)	89	11.63	2.9	3.521
QB2000-330	20:03:24.0	−32:51:44	3.773	14(14)	80	11.67	2.9	3.725
Q1621-0042	16:21:16.9	−00:42:50	3.709	12(11)	105	11.55	2.9	3.662
Q1317-0507	13:20:30.0	−05:23:35	3.700	22(20)	97	11.57	2.9	3.653
Q0055-269	00:57:58.1	−26:43:14	3.655	12(12)	82	11.66	2.9	3.608
Q1422+23	14:24:38.1	+22:56:01	3.620	8(8)	217	11.24	2.9	3.574

Notes – 1: Name of the quasar sightline; 2 & 3: RA and Dec of the quasar (J2000); 4: redshift of the quasar; 5: Total number of LAEs detected in MUSE. The number in parentheses indicates the number of LAEs for which we have C IV coverage outside the LAF region and free from significant skyline contamination; 6: Median SNR of the quasar spectrum at $6657 \pm 100 \text{ \AA}$; 7: Limiting C IV column density at the median SNR of the respective sightlines for a typical gas temperature of $\approx 10^4 \text{ K}$; 8: The minimum redshift probed; 9: The maximum redshift of interest, $z_{\text{max}} = z_{\text{qso}} - (1 + z_{\text{qso}}) \times \frac{3000}{c}$.

by MUSE, whereas the upper bound is determined by the redshift of the most distant quasar in our sample. Quasars at $z > 4$ were avoided deliberately in MUSEQuBES since the Ly α forest (LAF) regions become too crowded to obtain accurate H I column densities.

This paper is organized as follows. In Section 2 we briefly describe our C IV absorber and LAE catalogs. In Section 3 we present our analysis and results. In Section 4, we discuss our results and compare them with the literature, followed by the conclusions in Section 5. Throughout this study, we adopted a flat Λ CDM cosmology with $H_0 = 70 \text{ km s}^{-1} \text{ Mpc}^{-1}$, $\Omega_{\text{M}} = 0.3$ and $\Omega_{\Lambda} = 0.7$, and all distances given are in physical units unless specified otherwise.

2 DATA

2.1 Quasar spectra and the “blind” C IV absorber catalog

The quasar spectra used in this study are the same as presented in Muzahid et al. (2021, see Section 2.2). Briefly, for all 8 quasars, we have excellent quality optical spectra obtained with the VLT/UVES and/or Keck/HIRES spectrographs with a resolving power of $R \approx 45,000$. All but one spectrum have a signal-to-noise ratio (SNR) of > 70 per pixel in the region red-wards of the quasars’ Ly α emission (see Table 1). The corresponding limiting rest-frame equivalent width (REW) is 0.0015 \AA (the limiting C IV column density is $\log_{10} N(\text{C IV})/\text{cm}^{-2} = 11.6$) for a gas temperature of $\sim 10^4 \text{ K}$.

We searched for C IV absorbers in these 8 spectra manually using the so-called doublet matching technique, which relies on the fact that the observed wavelength ratio of the two members of the C IV doublet ($\lambda\lambda 1548, 1550$) is equal to the ratio of their rest-frame wavelengths. We started by shifting the wavelength array of a given spectrum by the ratio of the rest-frame wavelengths of the C IV doublet and plotting the shifted spectrum on top of the original spectrum. We then inspected all the coincidences of lines between the original and shifted spectra redward of the Ly α forest.

While searching for C IV absorbers using this method, we

verified that (i) the overall shape of the C IV $\lambda 1548$ line is similar to the C IV $\lambda 1550$ line, and (ii) in the optically thin regime the C IV $\lambda 1548$ line will be ≈ 2 times stronger than the C IV $\lambda 1550$ line, provided that the lines are free from significant contamination (which is true for most of the C IV absorbers in our sample). However, whenever possible, we determined the identities of the interlopers if present.

Since our ultimate goal is to cross-match the blind C IV catalog with the catalog of LAEs detected in these fields (Muzahid et al. 2020, 2021), we did not include the C IV absorbers at $z < 2.9$, since no LAEs can be detected with MUSE below $z = 2.9$. Moreover, we excluded any absorbers detected within the quasar’s proximate zones, i.e., 3000 km s^{-1} blue-ward of the quasars’ redshifts, from our analysis.

Once the search is complete, an initial catalog of C IV absorbers was created. Next, we fit the Voigt profile of every C IV absorber (both the doublets) using the VPFIT software (v12.2; Carswell & Webb 2014). VPFIT² returns the best-fitting redshift (z), column density (N), and Doppler parameter (b) of each C IV component of a given absorber, estimated using an iterative χ^2 minimization technique.

It is known that the number of components used in the Voigt profile decomposition of an absorber is subjective. We generally used the minimum number of components required to obtain a reduced χ^2 close to unity. For each absorber, we repeated the fitting procedure iteratively to obtain the best-fit parameters. In the case of a blended C IV absorber, we measured the absorption parameters from the uncontaminated doublet member. Our final C IV absorber catalog comprises ≈ 152 C IV systems comprising of 489 Voigt components in the redshift range $2.900 \leq z \leq 3.835$ (median $z = 3.260$). “Absorption systems” are defined by sorting all the component redshifts in a given spectrum obtained from the Voigt profile, and then grouping the components within $\pm 300 \text{ km s}^{-1}$ to each other starting from the lowest redshift component. The best-fit parameters for these components are presented in Table A1. Fig. 1 shows an example of our Voigt profile decomposition. The profiles in cyan represent individual C IV compo-

² <https://people.ast.cam.ac.uk/~rfc/>

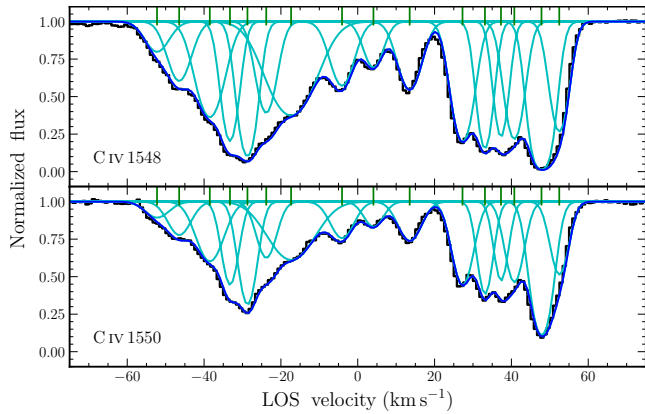


Figure 1. An example of Voigt profile decomposition using VPFIT. The C IV system is detected towards the sightline Q 1621–0042. The top and bottom panels show the C IV $\lambda 1548$ and C IV $\lambda 1550$ lines, respectively. The individual C IV components are shown in cyan and the resultant model profile is shown in blue. The green vertical ticks indicate the centroids of the individual C IV components. No contamination is present in this system.

nents. Their centroids are shown by the vertical green ticks. The resultant model C IV profile is shown in blue.

2.2 LAE catalog

The 96 LAEs in the redshift range $2.9 < z < 3.8$ used in this study are detected via their Ly α emission as part of our MUSEQuBES survey (P.I. Joop Schaye) (see Muzahid et al. 2020, 2021).³ MUSEQuBES consists of 8 MUSE pointings centered on the 8 UV-bright quasars with 50h of guaranteed time observations. The individual fields are observed for 2h – 10h with excellent seeing conditions (typically $< 0.8''$). The details of the MUSE observations and data reduction procedure are described in Sections 2.1 and 3.1 of Muzahid et al. (2021).

Line emitters in the 8 MUSE cubes are identified using CUBEX (v1.6; Cantalupo et al. 2018), and subsequently classified manually with the help of the 1D spectra and pseudo-narrow-band images. In total 96 objects were classified as LAEs. There are 9 LAEs (5 towards BRI1108–07, 2 towards Q 1317–0507, 1 each towards Q 1621–0042 and J 0124+0044) for which the corresponding C IV wavelengths are heavily affected by strong skylines. There is no C IV coverage for one of the LAEs detected towards PKS1937–101. We thus excluded these 10 LAEs from our analysis. The median redshift for the rest of the 86 LAEs is $z = 3.3$. The properties of these LAEs are summarized in Table 2.

It is well known that the Ly α emission peak is generally redshifted by a few hundred of km s^{-1} with respect to the systemic redshift of a galaxy. The Ly α peak redshifts of the 96 LAEs are corrected using the empirical relation $V_{\text{offset}} = 0.89 \times \text{FWHM} - 58 \text{ km s}^{-1}$ obtained in Muzahid et al. (2020) for our sample, where V_{offset} is the velocity offset between the Ly α emission peak and the systemic redshift and FWHM is the full width at half maximum of the Ly α line.

We estimated the halo mass (M_{vir}) and subsequently the

Table 2. Properties of the 86 LAEs in our sample.

Parameter	Min. ¹	Max. ²	Med. ³	N_{gal}
Redshift	2.918	3.814	3.306	86
Impact parameter (pkpc)	16.1	315.2	163.7	86
$\log_{10}(\text{SFR}/M_{\odot} \text{ yr}^{-1})$	-0.47	0.85	0.11	35
$\log_{10} L(\text{Ly}\alpha)/\text{erg s}^{-1}$ ^a	41.29	42.91	42.00	86
EW_0 (\AA) ^b	9.1	113.4	48.7	35
$\log_{10} M_{*}/M_{\odot}$ ^c	8.33	9.65	8.91	35
R_{vir} (pkpc) ^d	32.8	58.6	42.3	35

Notes– a: Ly α line luminosity; b: Rest-frame equivalent width of the Ly α emission line; c: Stellar mass; d: Virial radius. The values for SFR, EW_0 , stellar masses and virial radii are calculated using only the 35 out of 86 LAEs with robust SFR estimates (see text). ¹Minimum value, ²maximum value, and ³median value of the parameter.

R_{vir} for only those LAEs (35 out of 86) for which we could measure the star formation rate (SFR) from the UV continuum flux density (see Muzahid et al. 2020). Note that, these SFR values are dust-uncorrected and are calculated from the measured UV luminosity values using the local calibration relation of Kennicutt (1998) corrected to the Chabrier (2003) initial mass function. The halo masses (R_{vir}) range from $10^{10.97} - 10^{11.72} M_{\odot}$ (32.8 – 58.6 pkpc) with a median value of $10^{11.29} M_{\odot}$ (42.4 pkpc).

3 RESULTS

Our blind-absorber catalog of C IV absorption in the 8 high-resolution, high SNR quasar spectra contains 489 Voigt components (152 systems) in the redshift range $2.900 \leq z \leq 3.835$ (median $z = 3.260$). The redshift distribution of the components along each sightline is shown by the black histograms in Fig. 2. The sightlines are sorted in ascending order of the quasar redshifts, shown by the vertical dotted blue lines, from top to bottom. We excluded any absorbers within 3000 km s^{-1} of the quasars’ emission redshifts (horizontal green lines) in order to avoid the quasars’ proximity zones. The Q1422+23 sightline exhibits the highest number of C IV systems (25) likely because of the excellent SNR of the spectrum (Table 1). PKS1937–101 has the lowest number of systems (7) possibly due to the lack of sufficient spectral coverage shown by the blue horizontal line in Fig. 2.

The red star symbols in Fig. 2 indicate the redshifts of the 86 LAEs for which we have C IV coverage. The open cyan star symbols represent the 10 LAEs for which the data are heavily contaminated by skylines (no C IV coverage for one LAE towards PKS 1937–101). Note that there are some LAEs with no associated C IV absorbers. Similarly, for some of the absorbers, there are no nearby LAE counterparts.

3.1 Analyses of the “blind” C IV absorbers

3.1.1 Statistics of the C IV absorption components

In this section, we discuss the distributions and statistical properties of the Doppler parameter (b) and column density (N) of the C IV components obtained from the blind search

³ MUSEQuBES is a dual survey. For the low- z counterpart, see Dutta et al. (2023b).

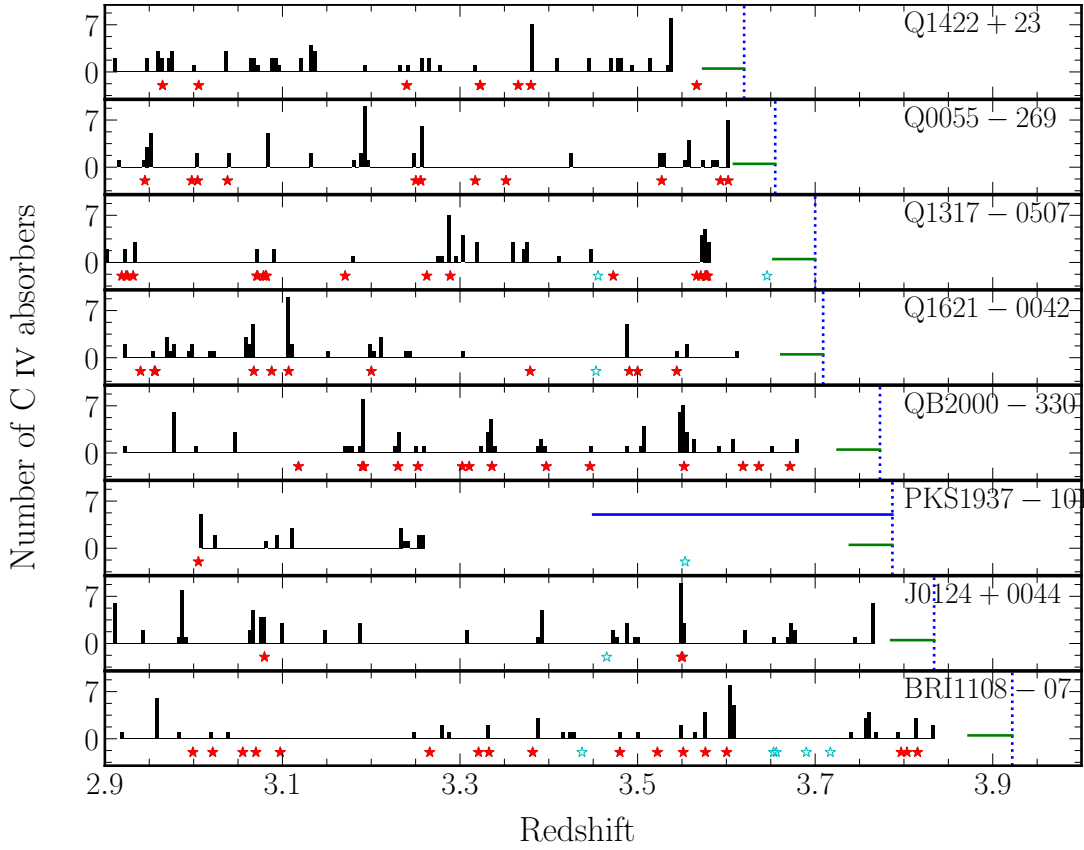


Figure 2. Histograms of the redshifts for the 489 C IV components obtained from Voigt profile fitting in bins of $\Delta z = 0.004$ (corresponding to 300 km s^{-1} at $z \approx 3$). The quasar sightlines are sorted in ascending order of the quasar redshifts indicated by the blue dotted lines from top to bottom. The 86 LAE redshifts in the different quasar sightlines are represented by the red star symbols, while the empty cyan stars represent the LAEs for which the C IV wavelengths are either severely affected by skylines or not covered. The green horizontal lines are the excluded 3000 km s^{-1} ranges blueward of the quasar redshifts. The blue horizontal line for PKS1937-101 indicates the lack of spectral coverage. Note that there are some LAEs without associated C IV absorbers. Similarly, for some of the absorbers, there are no nearby LAE counterparts.

(i.e., identified without any prior knowledge of the LAE catalog). The left panel of Fig. 3 shows the scatter plot of $N(\text{C IV})$ versus $b(\text{C IV})$ for all the C IV components in our sample. The distributions of the parameters are also shown on the side panels. The column density of the “blind” C IV “components” shows a range of $\log_{10} N(\text{C IV})/\text{cm}^{-2} = 11.4 - 14.3$ with a mean of 12.7 ± 0.5 (median 12.7). The mean and standard deviation of the column density distribution for the C IV “systems” is $\log_{10} N(\text{C IV})/\text{cm}^{-2} = 13.1 \pm 0.6$ (median 13.0) for our sample.

The b parameters range from $0.87 - 41.4 \text{ km s}^{-1}$, except for the one component with a very large b value (89 km s^{-1}) detected towards Q0055-269. We believe this outlier is owing to the poor continuum placement at the wavelength of the absorber. The mean value of the Doppler parameter for the complete sample is $13.6 \pm 8.0 \text{ km s}^{-1}$ (median 12.0 km s^{-1}). Considering pure thermal broadening, the median $b(\text{C IV})$ value corresponds to an upper limit on the gas temperature of $1.1 \times 10^5 \text{ K}$. Since this is close to the temperature at which C IV ionization fraction peaks under collisional ionization equilibrium, it is likely that the bulk of the C IV absorbers in our sample are photoionized (see also Muzahid et al. 2012).

The blue dot-dashed line in Fig. 3 represents the 3σ detection limit corresponding to the median SNR of 50 per pixel. It

indicates the maximum C IV column density that can be hidden within the 3σ noise of the spectrum for a given Doppler parameter. The column density upper limits are estimated from the limiting equivalent width (W_{lim}) for the C IV $\lambda 1550$ line assuming the linear part of the curve-of-growth relation.⁴ The W_{lim} is calculated using the following equation from Hellsten et al. (1998):

$$W_{\text{lim}} = \frac{N_{\sigma} \sqrt{N_{\text{pix}}} \Delta\lambda_{\text{pix}}}{\text{SNR} (1 + z_{\text{abs}})}, \quad (1)$$

where, $N_{\sigma} (= 3)$ is the detection threshold, $\Delta\lambda_{\text{pix}}$ is the pixel size in Å, SNR is the signal-to-noise ratio per pixel, and N_{pix} is the number of pixels contributing to the unresolved absorption. Note that N_{pix} depends on the assumed b -parameter. For a given b value, we first calculate the σ of the Line Spread Function (LSF) convolved line (i.e., $\sigma^2 = \sigma_{\text{lsf}}^2 + \sigma_{\text{line}}^2$). The

⁴ Note that we used the weaker member of the C IV doublet in this calculation which provides a conservative upper limit. This is because of the fact that our visual identification technique relies on the detection of both the C IV doublet members. However, in case of contamination, we used the $\lambda 1548$ line and scaled the W_{lim} measurement to the one corresponding to the $\lambda 1550$ line.

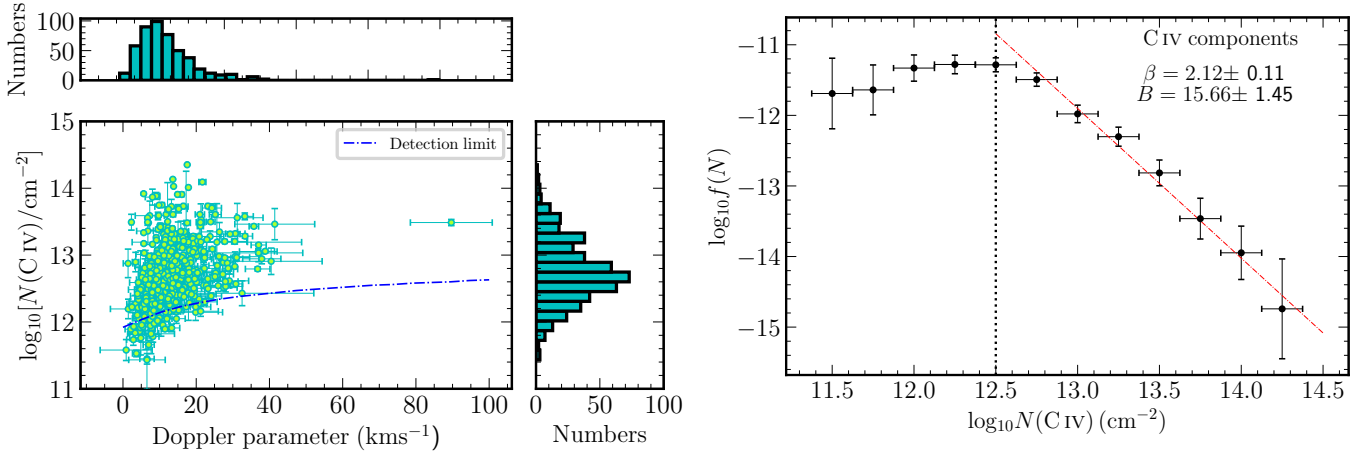


Figure 3. *Left:* Best-fit values of column density and Doppler parameter of all the C IV absorption components. The distributions of the respective parameters are shown in the side panels. The blue dashed line indicates the maximum $N(\text{C IV})$ that can be hidden within the average 3σ noise of the spectra for a given Doppler parameter (see the text for details). The median Doppler parameter of individual C IV components is 12.0 km s^{-1} and median column density is $\log_{10} N/\text{cm}^{-2} = 12.7$. The median value of column density of C IV systems is $\log_{10} N/\text{cm}^{-2} = 13.0$, where the linking velocity used to define a system is 300 km s^{-1} . A correlation is found between the $N(\text{C IV})$ and $b(\text{C IV})$. *Right:* The CDDF for individual C IV components. The error bars along the y-axis indicate the 1σ Poisson errors. Along the x-axis, the error bars represent the bin size (0.25 dex). The best-fit power-law relation, shown by the red dot-dashed line, is obtained using non-linear least squares fitting for the data points rightwards of the vertical dotted line at $\log N/\text{cm}^{-2} = 12.5$, below which our survey suffers from incompleteness.

N_{pix} is then determined by counting the number of pixels within the FWTM (full width at tenth maximum).

A correlation is seen between the column density and Doppler parameter of the C IV components for the full sample (with Spearman rank correlation coefficient $\rho_s = 0.41$, $p\text{-value} = 4.2 \times 10^{-21}$) and for the C IV components above the detection limit curve ($\rho_s = 0.37$, $p\text{-value} = 6.5 \times 10^{-16}$).

3.1.2 Column Density Distribution Function

The column density distribution function (CDDF), $f(N)$, is defined as the number of absorbers (either individual components or systems) per unit column density per unit redshift range. The CDDF can be parameterized as $f(N)dN = BN^{-\beta}dN$, where β and B are the power-law index and normalization, respectively.

The *right* panel of Fig. 3 depicts the CDDF for individual C IV components for our survey with a total redshift path length of $\Delta z = 6.20$. The plot also shows the best-fit power-law model.⁵ We obtained best-fit values of $\beta = 2.12 \pm 0.11$ and $B = 15.66 \pm 1.45$. The fitting is performed for $\log_{10} N(\text{C IV})/\text{cm}^{-2} > 12.5$ below which our survey suffers from incompleteness. The β value obtained for the C IV systems is 1.77 ± 0.17 (plot not shown). The shallower power-law slope for systems is expected as multiple low-column density components are added to construct a system. Finally, we note that our β values are consistent with earlier estimations at $z \gtrsim 2$ in the literature (e.g., Songaila 2001; Ellison et al. 2000; D’Odorico et al. 2010; Muzahid et al. 2012).

3.2 Linking the LAEs and the C IV absorbers

We have so far discussed the properties of the C IV absorbers detected via a blind search. Now we will focus on the properties of the C IV absorbers associated with LAEs.

The blue histogram in Fig. 4 shows the line of sight (LOS) velocity distribution of the individual C IV components detected within $\pm 1500 \text{ km s}^{-1}$ of the LAEs. The zero velocity ($\Delta v = 0 \text{ km s}^{-1}$) corresponds to the redshift of the LAEs. It is evident from the figure that the number of C IV components is enhanced near $\approx 0 \text{ km s}^{-1}$. The best-fit Gaussian + baseline model (black solid line) returns a σ of $\approx 165 \pm 110 \text{ km s}^{-1}$, corresponding to an FWHM of $\approx 390 \text{ km s}^{-1}$. This indicates a velocity-correlation between the LAEs and C IV absorbers within $\approx \pm 400 \text{ km s}^{-1}$.⁶ The grey-shaded histogram in Fig. 4 shows the LOS velocity distribution of “random” C IV absorbers. The “random” sample is constructed by generating 1000 uniform random numbers along each sightline within the corresponding z_{min} and z_{max} values listed in Table 1. We will refer to these 8000 redshifts as the “random sample” throughout this paper. As expected, no clustering is seen for the LOS velocity distribution for this random sample.

Next, we explored that the high column density absorbers (i.e., $\log_{10} N/\text{cm}^{-2} > 13.0$) are more tightly correlated with the LAEs in velocity with a σ value of $\approx 136 \text{ km s}^{-1}$ (FWHM $\approx 320 \text{ km s}^{-1}$; see Fig. A.1 left panel). We also inspected the $N(\text{C IV})$ -weighted LOS velocity distribution of the C IV absorbers within $\pm 1500 \text{ km s}^{-1}$ of the LAEs. A similar Gaussian + baseline fit returned a significantly smaller σ value of $\approx 62 \text{ km s}^{-1}$. This indicates that the higher column density C IV absorbers are more tightly correlated to the LAEs. We confirmed that these results are insen-

⁵ We used the CURVE-FIT package of PYTHON which returns the best-fit parameters based on the non-linear least-squares method.

⁶ The errors on the μ and σ values indicated in the plot are estimated using 1000 bootstrap realizations.

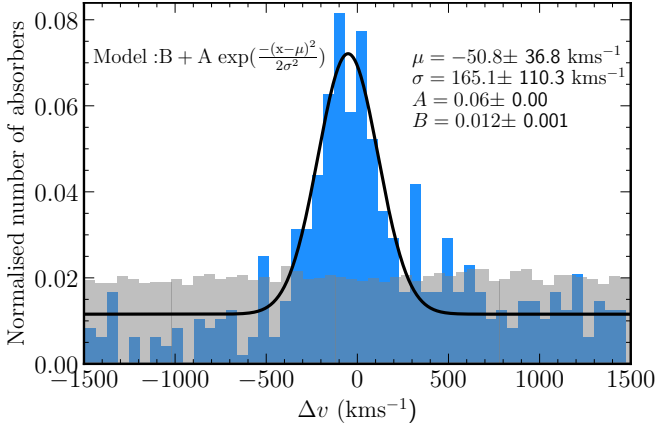


Figure 4. The LOS velocity distribution of all the C IV components within $\pm 1500 \text{ km s}^{-1}$ of the LAE redshifts (corresponding to 0 km s^{-1}) is shown by the blue histogram. The grey shaded histogram shows the same but for the random sample (see text). The number of C IV components is enhanced near the 0 km s^{-1} . We fit the distribution of the entire sample (black solid line) using a Gaussian+Linear model. The best-fit parameters of the model indicate an excess of C IV components compared to a random region within 165 km s^{-1} , which corresponds to an FWHM of $\approx 400 \text{ km s}^{-1}$.

sitive to the velocity range (i.e. $\pm 1500 \text{ km s}^{-1}$) we considered here. Hence, analyzing the absorbers within $\pm 500 \text{ km s}^{-1}$ of the LAEs would be sufficient to study the interplay between metal-rich gas and low-mass galaxies at high- z .

Out of the 489 C IV components 202 lie within $\pm 500 \text{ km s}^{-1}$ of the 86 LAE redshifts. We found that the column density and Doppler parameter distributions of these 202 C IV components are not statistically different compared to the remaining 287 components (p -values from two-sided KS-tests > 0.05). The median C IV column density ($\log_{10} N(\text{C IV})/\text{cm}^{-2} \approx 12.7$) and b -parameter ($\approx 12.0 \text{ km s}^{-1}$) of the two samples are also consistent with each other. These facts suggest two possibilities: (i) a fraction of the absorbers that are unrelated to the detected LAEs are related to fainter galaxies below our detection thresholds and/or (ii) not all the associated C IV components (i.e., within $\pm 500 \text{ km s}^{-1}$ of the LAEs) are actually physically related to the LAEs.

Fig. 5 shows the LOS velocity of the C IV components detected within $\pm 500 \text{ km s}^{-1}$ of the LAEs as a function of the impact parameter of the respective LAEs. A Spearman rank correlation test suggests no specific trend between these two parameters ($\rho_s = 0.08$ and p -value = 0.25). The points are color-coded by their column densities. The black shaded region shows the escape velocity at different distances for the halo mass range covered by our LAE sample, i.e., $10.96 \leq \log_{10} M_h/M_\odot \leq 11.72$. The black dashed line indicates the same for the median halo mass of our sample ($\log_{10} M_h/M_\odot = 11.29$). To draw these curves, we used the relation, $v_{\text{esc}} = \sqrt{\frac{2GM_h}{R}}$, and assumed that the impact parameter is the same as the 3D distance (R) from the center of the halo.

Out of the 202 C IV components detected within $\pm 500 \text{ km s}^{-1}$ of the LAE redshifts 111 ($\approx 55\%$) fall inside this shaded region. It is safe to say that the absorbers falling beyond the shaded region are not bound to the LAEs. How-

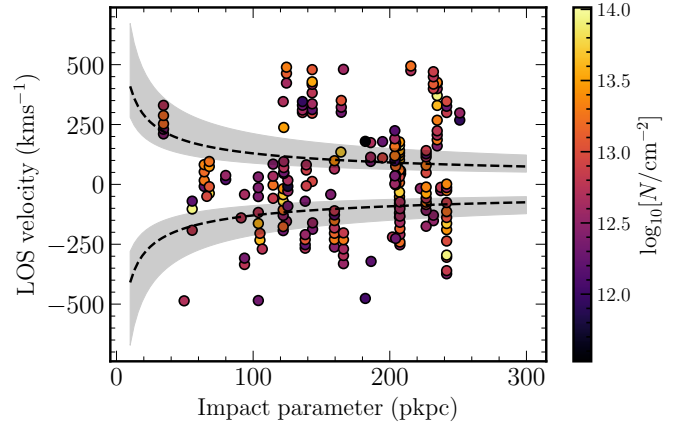


Figure 5. The LOS velocity of the C IV components residing within $\pm 500 \text{ km s}^{-1}$ of the LAEs as a function of the impact parameter of the respective LAEs. The points are color-coded by their respective column densities. The escape velocity as a function of distance for a halo mass range encompassed by our LAE sample i.e. $10.96 \leq \log_{10} M_h/M_\odot \leq 11.72$, is indicated by the black shaded region. The black dashed line indicates the same for the median halo mass of our sample ($\log_{10} M_h/M_\odot = 11.29$). Roughly 45% of the C IV absorbers residing within $\pm 500 \text{ km s}^{-1}$ of the LAEs are not bound.

ever, interpreting the nature of the absorbers within the v_{esc} bounds is not straightforward since the impact parameter and LOS velocity of an absorber are merely lower limits on the actual 3D distance and velocity, respectively. Nevertheless, from now on, we will refer to these components as “bound absorbers”.

We did not find any significant difference between the column density of “bound absorbers” (111 components) and the remaining “unbound absorbers” (378 components) ($D_{KS} = 0.14$ and p -value = 0.25). The same holds for the Doppler parameter distributions ($D_{KS} = 0.16$ and p -value = 0.12). The median C IV column densities for the bound and unbound components are $\log_{10} N/\text{cm}^{-2} = 12.8$ and 12.7 respectively, and the median Doppler parameters are 12.4 and 10.9 km s^{-1} .

We take into consideration the fact that the LOS velocity depends on the systemic redshifts of the LAEs. The systemic redshifts are calculated from the Ly α redshifts using the empirical relation provided in Muzahid et al. (2020). We confirmed that there is no correlation between the LOS velocities of various C IV components and the velocity offsets applied to correct the Ly α redshifts. This ensures that there is no systematic uncertainty, related to the scatter in the empirical relation, in determining the nature of the absorbers (i.e., unbound vs. bound).

Finally, we reconstructed Fig. 4 using only the bound components (see right panel of Fig. A.1). The line centroid of the best-fit model ($\mu = -35.7 \pm 33.3 \text{ km s}^{-1}$) is consistent with $\Delta v \approx 0 \text{ km s}^{-1}$ while in Fig. 4 we noted a $\approx 1.4\sigma$ offset ($\mu = -50.8 \pm 36.8 \text{ km s}^{-1}$) with respect to the systemic redshift. Note that, Muzahid et al. (2021) also found an offset of $-30 \pm 22 \text{ km s}^{-1}$ between their stacked C IV profile and the systemic redshifts of LAEs. The best-fit σ of 105 km s^{-1} obtained from the plot corresponds to an FWHM of $\approx 247 \text{ km s}^{-1}$. As a result, for the majority of our analysis, we focused on a velocity window of $\pm 250 \text{ km s}^{-1}$.

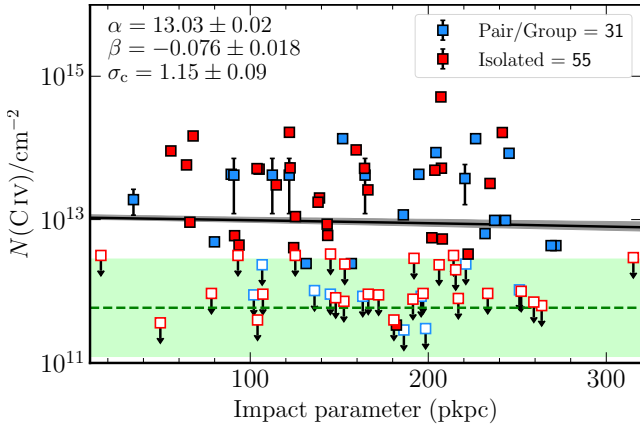


Figure 6. The total C IV column density as a function of impact parameter. The solid squares represent the total $N(\text{C IV})$ measured within $\pm 250 \text{ km s}^{-1}$ of the LAEs. The open squares with downward arrows indicate 3σ column density upper limits for the LAEs without detectable C IV absorption within $\pm 250 \text{ km s}^{-1}$. The black solid line shows the best-fit log-linear model, and the grey-shaded region shows the 1σ uncertainty of the fitted curve. This uncertainty does not consider the intrinsic scatter of the plot. No significant correlation exists between total $N(\text{C IV})$ and ρ . The green dashed line and the green shaded region represent the mean $N(\text{C IV})$ including the contribution from upper limits using the Kaplan-Meier estimator and 1σ scatter obtained for the random sample. The $N(\text{C IV})$ values measured near the LAEs are significantly higher compared to the random sample.

3.2.1 C IV column density profile

One of the main objectives of this work is to probe the radial variations of the C IV line parameters in the CGM of the high- z , low-mass galaxies. In this section, we will investigate the variation of C IV column density as a function of the impact parameter (ρ). In the previous section, we observed an enhancement of C IV components around the systemic redshifts of the LAEs out to a few hundred km s^{-1} (see Fig. 4), indicating a connection between the galaxies and the metal-enriched gas around them. In Fig. 6 we present the distribution of total C IV column density within a $\pm 250 \text{ km s}^{-1}$ velocity window against the impact parameter for the 86 LAEs in our sample. In cases where no C IV component is found, we obtained 3σ upper limits on $N(\text{C IV})$ using the method described in section 3.1.1 for the SNR measured near the C IV 1550 Å line. When the 1550 Å line is contaminated, we used the 1548 Å line to calculate the upper limit of equivalent width and then calculated the column density upper limit corresponding to the 1550 Å line using the relation of the linear part of the curve-of-growth. We assumed that the undetected line has a Doppler parameter of 12.0 km s^{-1} (median b of our “blind” components) in order to calculate the N_{pix} term in Eq. 1. The upper limits on the C IV column density are shown as downward arrows in the plot.

The horizontal green dashed line in Fig. 6 shows the median column density measured for the random sample. The green-shaded region shows the corresponding 1σ scatter. For each random redshift, we determined the total C IV column density using our “blind” catalog within $\pm 250 \text{ km s}^{-1}$. In the absence of any detected C IV component, we estimated the 3σ column density upper limit. Using the empirical cumulative distribution function (ECDF) for censored data (in the

Table 3. Best-fit parameters for log-linear fit to the C IV column density profile

$dv \text{ (km s}^{-1}\text{)}$	α	β	σ
± 500	13.04 ± 0.03	-0.068 ± 0.023	1.06 ± 0.10
± 300	13.03 ± 0.02	-0.074 ± 0.019	1.14 ± 0.10
± 250	13.03 ± 0.02	-0.076 ± 0.018	1.15 ± 0.09
± 150	13.02 ± 0.02	-0.082 ± 0.013	1.26 ± 0.13

presence of upper limits) using the Kaplan-Meier estimator⁷, we calculated the mean C IV column density for the random sample as $\log_{10} N(\text{C IV})/\text{cm}^{-2} = 11.77$ with a 1σ scatter of 0.68 dex. The vast majority of the C IV components within the $\pm 250 \text{ km s}^{-1}$ of the LAE redshifts show considerably higher column densities compared to the median C IV column density observed for the random sample. A two-sided logrank test⁸ suggests that the observed C IV column density distribution around the LAEs is significantly different than the random regions with a p -value of $< 10^{-7}$.

While the C IV column densities observed near the LAE redshifts are significantly higher than random regions, no significant trend is seen between the C IV column density and impact parameter. A Kendall’s τ rank-order correlation test, which takes care of the upper limits, suggests no significant anti-correlation between the total column density within $\pm 250 \text{ km s}^{-1}$ of the LAEs and impact parameter with a $\tau_K = -0.08$ and a p -value of 0.25⁹. This is also true for the absorbers within $\pm 500 \text{ km s}^{-1}$ of the LAEs ($\tau_K = -0.09$ and p -value = 0.21).

Following Chen et al. (2010, see also Nielsen et al. (2013)) we characterized the dependence between column density and ρ (in pkpc) assuming a log-linear model described as:

$$\log_{10} N(\text{C IV}) = \alpha + \beta \left(\frac{\rho}{160 \text{ pkpc}} \right). \quad (2)$$

To determine the values of the model parameters (α , β), we used the following maximum-likelihood function that takes care of both n number of measurements and m number of upper limits:

$$\mathcal{L}(N) = \left(\prod_{i=1}^n \frac{1}{\sqrt{2\pi\sigma_i^2}} \exp \left\{ -\frac{1}{2} \left[\frac{N_i - N(\rho_i)}{\sigma_i} \right]^2 \right\} \right) \times \left(\prod_{i=1}^m \int_{-\infty}^{N_i} \frac{dN'}{\sqrt{2\pi\sigma_i^2}} \exp \left\{ -\frac{1}{2} \left[\frac{N' - N(\rho_i)}{\sigma_i} \right]^2 \right\} \right),$$

where, N_i is the sum of the individual component column densities within $\pm 250 \text{ km s}^{-1}$ or the 3σ upper limit, and $N(\rho_i)$ is the expected value of $\log_{10} N(\text{C IV})$ from the model (Eq. 2) for individual ρ . The total error, $\sigma_i = \sqrt{\sigma_c^2 + \sigma_{mi}^2}$; with σ_{mi} denoting the error associated with i th measurement and σ_c accounting for the intrinsic scatter. The best-fit parameters of Eq. 2 calculated for different velocity windows are given in Table 3. These parameters are obtained using the

⁷ We used the CENFIT function under the NADA package in R. However, in this instance, rather than being randomly distributed, the censored data points are almost always lower compared to the detected values.

⁸ Performed using the SURVIVAL package in R.

⁹ We used the CENKEN function under the NADA package in R.

Table 4. Kendall’s τ correlation test results between $N(\text{C IV})$ and ρ

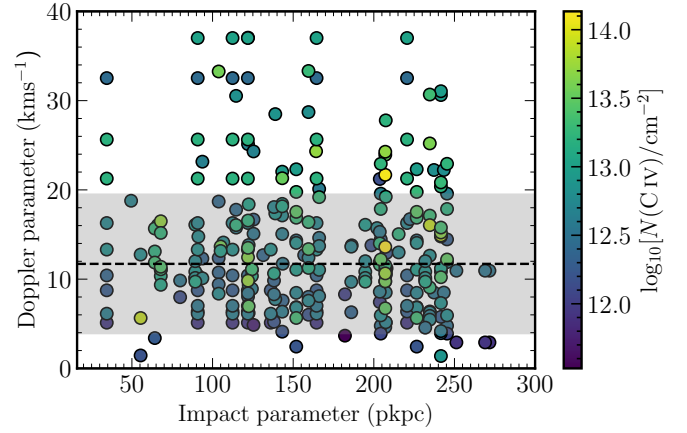
Sample (No. of LAEs)	τ_K	p -value
All (86)	−0.09	0.21
Pair/Group (31)	−0.06	0.67
Isolated (55)	−0.14	0.14

nested sampling Monte Carlo algorithm MLFriends (Buchner 2014, 2019) using the UltraNest¹⁰ package of Python (Buchner 2021). The best-fit slope (e.g., -0.076 ± 0.018 for $\pm 250 \text{ km s}^{-1}$) with a large scatter ($\sigma_c = 1.15 \text{ dex}$) clearly rules out any strong trend between $N(\text{C IV})$ and the impact parameter. To cross-verify our results, we used the Python `linmix` package (Kelly 2007)¹¹, which employs a hierarchical Bayesian model for fitting a straight line to data. We found the best-fit values as $\alpha = 12.83 \pm 0.44$, $\beta = -0.44 \pm 0.41$, and $\sigma_c = 1.79 \pm 0.47$. Despite the fact that α and σ_c are consistent with previous values, the β value is different here. The β value returned by `linmix` is consistent with zero within 1σ significance, which further confirms the absence of any strong trend as suggested by Kendall’s τ tests.

The data points in Fig. 6 are color-coded by the environments (“isolated” or “pair/group”) of the LAEs. To define the environment, we used the procedure followed by Muzahid et al. (2021). We defined a galaxy pair/group in such a way that each member of a pair/group has at least one companion within $\pm 500 \text{ km s}^{-1}$ and within the MUSE FoV ($\approx 300 \text{ pkpc}$ on a side). These conditions are met by 31 out of our 86 galaxies. The rest are classified as “isolated” galaxies. Muzahid et al. (2021) argued that detecting 2 LAEs within $\pm 500 \text{ km s}^{-1}$ within the MUSE FoV corresponds to a galaxy overdensity of ≈ 10 . The blue squares represent the $N(\text{C IV})$ for the pair/group LAEs whereas the red squares are for the isolated LAEs. It is readily apparent that the bulk of the upper limits on $N(\text{C IV})$ (non-detections) arises from the isolated systems. Specifically, $\approx 44\%$ of the isolated LAEs (24 out of 55) show upper limits, whereas only $\approx 17\%$ (5 out of 29) of the pair/group LAEs exhibit C IV non-detection. This hints at a higher C IV covering fraction for the pair/group galaxies compared to the isolated LAEs. We further investigate this in Section 3.2.6

Next, we fit the log-linear relation (Eq. 2) separately for isolated and pair/group galaxies. The slopes, intercepts, and scatter for the isolated and pair/group subsamples are consistent with each other and with the full sample. The lack of a strong trend for these two subsamples is also apparent from the Kendall’s τ results summarised in Table 4 (for column density measured within $\pm 500 \text{ km s}^{-1}$). On a passing note, we also looked for any correlation between column density and LOS velocity from the LAE and did not find anything significant (Spearman correlation test result: $\rho_s = -0.06$, p -value=0.4).

Finally, we note that the fraction of pair/group LAEs increases with the impact parameter. For example, from 0–100 pkpc, the fraction is $\frac{4}{14}$ (pair/group-4, isolated-10); from 100–200 pkpc, the ratio becomes $\frac{16}{44}$ (pair/group-16, isolated-28); and from 200–300 pkpc, it is $\frac{11}{28}$ (pair/group-11, isolated-17).

**Figure 7.** Doppler parameter of the C IV components within $\pm 500 \text{ km s}^{-1}$ from the LAEs against impact parameter. The data points are color-coded by their column densities as indicated by the color bar. The black dashed line and gray shaded region are the median value of the Doppler parameter and its 1σ scatter for the random sample. No significant correlation exists between $b(\text{C IV})$ and ρ .

This can be attributed to the “edge effect” owing to the limited FoV of MUSE. A pair/group LAE can be confused with an isolated LAE because the companion LAE is just outside the MUSE FoV.

3.2.2 C IV Doppler parameter profile

Fig. 7 shows the b -parameters of individual C IV components associated with the LAEs as a function of the impact parameter, color-coded by the column density, detected within $\pm 500 \text{ km s}^{-1}$ from the LAEs. It seems there is no significant trend between $b(\text{C IV})$ and ρ . This visual impression is also supported by the Spearman rank correlation test results summarized in Table 5. Since we observed a mild correlation between $N(\text{C IV})$ and b in Section 3.1.1, we split the sample into three different column density bins and performed the Spearman tests between $b(\text{C IV})$ and ρ for each of these three column density bins (see Table 5). The table also includes the correlation test results for the pair/group and isolated LAEs separately. The overall trend suggests the $b(\text{C IV})$ and impact parameters of C IV components are not significantly correlated for any of the subsamples except maybe for the lowest column density bin (p -value = 0.03). Similarly, no significant correlation was found between b and the LOS velocity of the C IV components with respect to the LAEs (Spearman correlation test result: $\rho_s = -0.02$, p -value=0.7).

We also generated a random sample of Doppler parameters considering all the C IV components within $\pm 500 \text{ km s}^{-1}$ of our random redshifts described in section 3.2. In case of a non-detection, we considered the b value of the nearest detected C IV component to that random redshift. We obtained a median of 11.7 km s^{-1} and a standard deviation of 7.7 km s^{-1} for the random sample which are shown by the black dashed line and the grey-shaded region, respectively, in Fig. 7. A KS test between the b -distributions of the CGM sample and the random sample gives $D_{KS} = 0.07$ and p -value = 0.12. This suggests these two populations are not statistically different.

¹⁰ <https://johannesbuchner.github.io/UltraNest/>

¹¹ <https://github.com/jmeyers314/linmix>

Table 5. Spearman rank correlation test results between b and impact parameter for the C IV components

Sample ¹	Number ²	ρ_s^3	p -value ⁴
All	303	-0.08	0.15
$11.5 \leq \log_{10} N/\text{cm}^{-2} < 12.5$	80	-0.24	0.03
$12.5 \leq \log_{10} N/\text{cm}^{-2} < 13.0$	127	-0.13	0.15
$13.0 \leq \log_{10} N/\text{cm}^{-2} < 14.5$	96	+0.04	0.67
Related to Pair/Group LAEs	151	-0.09	0.27
Related to Isolated LAEs	152	-0.08	0.32

Notes–1: C IV sample, based on column density and environment; 2: Number of C IV components contributing to the sample. Note that, the total number of C IV components in sample “All” is greater than the number of components present within $\pm 500 \text{ km s}^{-1}$ of the LAEs (202) because closely spaced LAEs will share some of the C IV components with each other, so some of the components will contribute multiple times; 3: Spearman rank correlation coefficient; 4: Probability that there is no correlation.

3.2.3 C IV covering fraction

Covering fractions of different atomic and ionic species in the CGM of galaxies are a measure of the patchiness of the medium and metal distribution, and provide stringent constraints on galaxy evolution models. In this section, we determine the C IV covering fraction in the neighbourhood of the LAEs in our sample. For a given threshold column density, N' , the covering fraction (f_c) is defined as:

$$f_c = \frac{n_{\text{Hit}}(N \geq N')}{n_{\text{Total}}},$$

where, n_{Hit} is the number of LAEs with a total column density $N \geq N'$, measured within a specific LOS velocity window around the LAEs, and n_{Total} is the total number of LAEs for which the spectra were sensitive enough to detect absorption down to the threshold column density of N' .

To determine the C IV covering fraction, we first calculated the 3σ limiting column density for each LAE in our sample using the SNR of the corresponding quasar spectra near the expected C IV wavelengths (preferably at 1550 \AA) following the procedure described in Section 3.2.1. Fig. 8 shows the covering fraction of C IV as a function of threshold column density, for two different LOS velocity windows around the LAEs. The black (magenta) dots correspond to the measurements within $\pm 500 \text{ km s}^{-1}$ ($\pm 250 \text{ km s}^{-1}$) of the LAEs. The C IV covering fraction calculated for the entire impact parameter range of $16 - 320 \text{ pkpc}$ of our LAEs is close to 60% for a threshold column density of $10^{12.5} \text{ cm}^{-2}$, but declines to $\approx 10\%$ for strong C IV absorbers with $N(\text{C IV}) > 10^{14.0} \text{ cm}^{-2}$. The cyan squares in Fig. 8 show the covering fraction estimated using the bound absorbers for a velocity window of $\pm 250 \text{ km s}^{-1}$. The C IV covering fraction for the bound absorbers alone is as high as $\approx 50\%$ for a threshold column density of $10^{12.5} \text{ cm}^{-2}$. We have also estimated the same for different absorber and galaxy sub-samples using different velocity windows in the following sections. All the measurements are summarized in Table 6.

We also estimated C IV covering fraction at random locations using the random sample. In Fig. 8, the colored empty dots are the covering fraction for this random sample calcu-

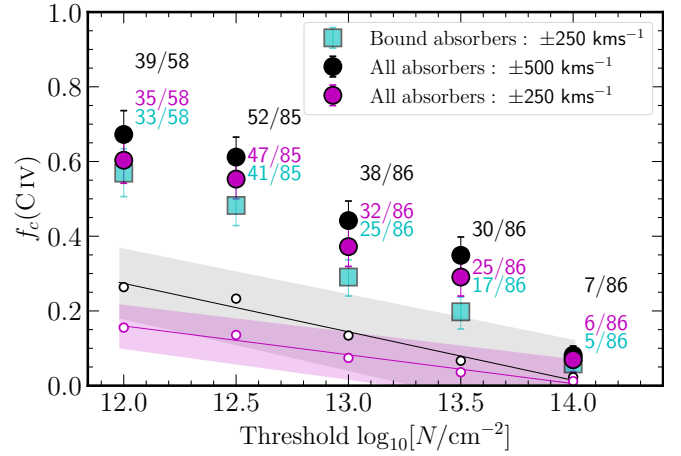


Figure 8. The C IV covering fraction (f_c) within $16-315 \text{ pkpc}$ of the LAEs for different threshold column densities. The filled circles indicate the covering fraction calculated using all the absorbers within the LOS velocity separations from the LAEs indicated by the legends. The cyan squares represent the covering fractions estimated using the bound absorbers only. The error bars in f_c are calculated using the binomial proportion confidence interval (BPCI) Wilson Score method. The n_{Hit} and n_{Total} for each measurement are indicated by the numbers in the numerator and denominator of similar colors adjacent to the points. The black and magenta small open circles represent the C IV covering fractions measured for the random sample for ± 500 and $\pm 250 \text{ km s}^{-1}$ velocity windows, respectively. The solid lines represent the corresponding best-fit linear relations between the threshold column density and the f_c for the random sample, while the shaded regions represent the 1σ uncertainties.

lated within the LOS velocity ranges mentioned in legends. The solid lines are the best-fit straight lines while the shaded regions represent the 1σ uncertainties. It is worth noting that the probability of finding a C IV absorber is noticeably higher (more than twice) in the neighbourhood of the LAEs than in random locations for almost the entire range of column density probed here.

3.2.4 Redshift evolution of C IV covering fraction

In this section, we will examine whether the C IV covering fraction evolves with redshift. The cosmic time span of our sample is $\Delta t = 0.6 \text{ Gyr}$ for $z = 2.92$ to 3.82 and $\Delta z/(1+z_{\text{median}})$ is small (≈ 0.2), hence, we do not expect a strong redshift evolution. Fig. 9 shows the C IV covering fraction for the C IV absorber-sample within $\pm 250 \text{ km s}^{-1}$ of the LAEs for two redshift bins partitioned by the median redshift ($z \approx 3.3$). Here, we have chosen a threshold column density of $\log_{10} N/\text{cm}^{-2} = 12.5$.

To eliminate any possible environmental effects, we further calculated the covering fraction for only isolated LAEs, shown by the red points in Fig. 9. Similarly, the impact parameter controlled f_c measurements shown in cyan eliminate any possible effects due to the difference in the ρ distributions. For controlling the impact parameter, first, we split the LAEs into two redshift bins based on their median redshift, and then we chose the LAEs in such a way that for each LAE in the lower bin, there was a LAE in the upper bin with an impact parameter consistent within $\pm 10 \text{ pkpc}$. In all three cases (i.e., full sample, isolated sample, and impact-parameter

Table 6. Summary of C IV covering fraction measurements

Sample	Threshold $\log_{10} N/\text{cm}^{-2}$				
	12.0	12.5	13.0	13.5	14.0
All absorbers: ± 500	$0.77^{+0.11}_{-0.16}$	$0.64^{+0.05}_{-0.06}$	$0.44^{+0.05}_{-0.05}$	$0.35^{+0.05}_{-0.05}$	$0.08^{+0.03}_{-0.02}$
All absorbers: ± 250	$0.60^{+0.06}_{-0.06}$	$0.55^{+0.05}_{-0.05}$	$0.37^{+0.05}_{-0.05}$	$0.29^{+0.05}_{-0.05}$	$0.07^{+0.03}_{-0.02}$
All absorbers: ± 125	$0.52^{+0.06}_{-0.06}$	$0.41^{+0.05}_{-0.05}$	$0.28^{+0.04}_{-0.05}$	$0.19^{+0.04}_{-0.04}$	$0.05^{+0.02}_{-0.03}$
Bound absorbers: ± 250	$0.59^{+0.06}_{-0.06}$	$0.51^{+0.05}_{-0.05}$	$0.33^{+0.05}_{-0.05}$	$0.22^{+0.05}_{-0.04}$	$0.06^{+0.03}_{-0.02}$
Pair/Group LAEs: $d_{\text{cov}} = \pm 250$ $d_{\text{link}} = \pm 500$	--	$0.57^{+0.09}_{-0.09}$	$0.39^{+0.09}_{-0.09}$	$0.36^{+0.09}_{-0.08}$	--
Isolated LAEs: $d_{\text{cov}} = \pm 250$ $d_{\text{link}} = \pm 500$	--	$0.37^{+0.09}_{-0.08}$	$0.17^{+0.08}_{-0.06}$	$0.14^{+0.08}_{-0.05}$	--
Pair/Group LAEs: $d_{\text{cov}} = \pm 250$ $d_{\text{link}} = \pm 250$	--	$0.50^{+0.09}_{-0.09}$	$0.28^{+0.09}_{-0.08}$	$0.25^{+0.09}_{-0.07}$	--
Isolated LAEs: $d_{\text{cov}} = \pm 250$ $d_{\text{link}} = \pm 250$	--	$0.26^{+0.09}_{-0.07}$	$0.11^{+0.07}_{-0.04}$	$0.07^{+0.06}_{-0.03}$	--
Variable	dv	Type of LAEs	Covering fraction ^a		
Redshift, $z < 3.3$	± 250	All	$0.55^{+0.07}_{-0.08}$		
		Isolated	$0.46^{+0.09}_{-0.09}$		
		Controlled ρ	$0.53^{+0.09}_{-0.09}$		
Redshift, $z > 3.3$	± 250	All	$0.56^{+0.07}_{-0.07}$		
		Isolated	$0.57^{+0.09}_{-0.09}$		
		Controlled ρ	$0.55^{+0.09}_{-0.09}$		
$\rho : 16 - -100$ pkpc	± 250	All	$0.71^{+0.10}_{-0.13}$		
		Isolated	$0.60^{+0.14}_{-0.16}$		
$\rho : 100 - -200$ pkpc	± 250	All	$0.46^{+0.07}_{-0.07}$		
		Isolated	$0.52^{+0.09}_{-0.09}$		
$\rho : 200 - -315$ pkpc	± 250	All	$0.60^{+0.08}_{-0.09}$		
		Isolated	$0.47^{+0.12}_{-0.12}$		

Note– The errors in covering fraction are calculated using the binomial proportion confidence interval (BPCI) Wilson Score method.

^aThese values are calculated at threshold $\log_{10} N/\text{cm}^{-2} = 12.5$.

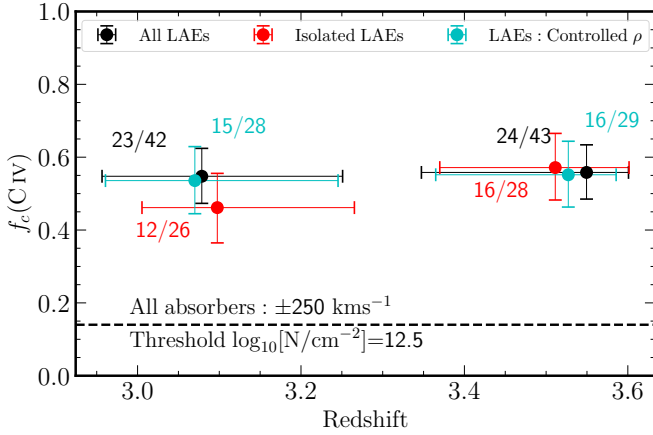


Figure 9. The redshift dependence of C IV covering fraction estimated using the absorbers within $\pm 250 \text{ km s}^{-1}$ of all LAEs (black), only for the isolated LAEs (red) and for the impact parameter controlled LAE sample (cyan). We have divided the LAE populations into two redshift bins based on their median redshifts. The calculations are done at a threshold $\log_{10} N/\text{cm}^{-2} = 12.5$. The x-position and error bar reflects the median value and the 16-84 percentile range. In all the cases, the values of f_c are consistent within 1σ , indicating no significant redshift evolution within our sample. The black dashed line indicates the covering fraction for a random sample at this threshold column density.

controlled sample), the covering fractions for the high- z and low- z bins are consistent within the 1σ allowed uncertainty, indicating no redshift evolution. Finally, no redshift evolution is seen even when we included all the associated components detected within $\pm 500 \text{ km s}^{-1}$ of an LAE redshift.

3.2.5 Environmental dependence of C IV covering fraction

In this section, we will investigate the effect of the galactic environment on the covering fraction of metal-rich gas traced by C IV. The top panel of Fig. 10 shows the C IV covering fraction for the pair/group and isolated LAEs for absorbers within $\pm 250 \text{ km s}^{-1}$ of the LAEs. Here we controlled for the impact parameter of the two subsamples in such a way that for each LAE in the isolated subsample, there is a galaxy in the pair/group subsample with an impact parameter consistent within $\pm 10 \text{ pkpc}$. In the previous section, we already found no significant redshift evolution of the C IV covering fraction. Additionally, it is unlikely that the SFR will influence the covering fraction as it covers a small dynamical range in our sample. Note that, for the threshold column density $\log_{10} N/\text{cm}^{-2} = 12.5$, the covering fraction for pair/group is $\approx 60\%$ whereas that of isolated LAEs is $\approx 40\%$. Moreover, we notice that even at a higher threshold of $\log_{10} N/\text{cm}^{-2} = 13.5$, the C IV covering fraction is quite high ($\approx 40\%$) for the pair/group galaxies compared to the isolated sample.

In the top panel, we defined a pair/group in such a way that each member of a pair/group has at least one companion within a linking velocity, dv_{link} of $\pm 500 \text{ km s}^{-1}$. If we use a dv_{link} of $\pm 250 \text{ km s}^{-1}$ instead of $\pm 500 \text{ km s}^{-1}$, the difference of C IV covering fractions between pair/group and isolated LAEs further increases for all the threshold column densities. This is shown in the bottom panel of Fig. 10. Here again, we considered the C IV components within $\pm 250 \text{ km s}^{-1}$ of the

LAEs (see Table 6). The enhancement of covering fraction is probably due to the fact that employing a wider velocity range for the group definition actually includes some isolated galaxies, which diminishes the environmental effect.

We investigated the environmental dependence of covering fraction using the median redshift of the group members to calculate the covering fraction for the pair/group galaxies. However, because of the small number of pairs/groups (10 for $dv_{\text{link}} = \pm 500 \text{ km s}^{-1}$ and 9 for $dv_{\text{link}} = \pm 250 \text{ km s}^{-1}$), the f_c values of the isolated and pair/group LAEs are not significantly different.

3.2.6 The C IV covering fraction profile

Our sample consists of galaxies with impact parameters ranging from 16.1 to 315.2 pkpc. Here we investigate the variation of the C IV covering fraction with the impact parameter. The black points in Fig. 11 show the covering fractions calculated in three bins of the impact parameter (0–100 pkpc, 100–200 pkpc, and 200–320 pkpc) for a threshold column density of $\log_{10} N/\text{cm}^{-2} = 12.5$ and a LOS velocity window of $\pm 250 \text{ km s}^{-1}$. The f_c for the innermost impact parameter bin is $\approx 71^{+0.10}_{-0.13}\%$. It declines to $\approx 46^{+0.07}_{-0.07}\%$ for the intermediate impact parameter bin but rises again for the outermost bin to $\approx 60^{+0.08}_{-0.09}\%$. Such an upturn, however, is not seen for the isolated galaxies (red points in the plot). This suggests that the upturn is indeed owing to the underlying environmental dependence.

The impact parameter normalized to the median virial radius of $\approx 42 \text{ pkpc}$ is shown along the top x-axis. The virial radius, R_{vir} or R_{200} , for an LAE is calculated from the halo mass as:

$$R_{200}^3 = 3M_{\text{halo}}/4\pi\Delta_{\text{vir}}\rho_c,$$

where $\Delta_{\text{vir}} = 200$ and ρ_c is the critical density of the universe at galaxy redshift. We first obtain the stellar masses from the UV SFR assuming that the LAEs lie on the star forming main sequence relation (Behroozi et al. 2019). The halo mass is then estimated from the halo abundance matching relation of Moster et al. (2013). Note that we could only estimate the virial radius for the 35 LAEs with SFR measurements. We would like to emphasize that even for the farthest bin, with $\rho > 200 \text{ pkpc}$ ($\geq 5R_{\text{vir}}$), the covering fraction of C IV around the isolated LAEs is significantly high ($\approx 50\%$).

In passing, we note that a similar analysis with the bound absorbers alone leads to similar conclusions. Finally, we did not find any significant dependence of the C IV covering fraction on the SFR, Ly α line luminosity ($L(\text{Ly}\alpha)$), or rest-frame equivalent width (EW_0) within the dynamical ranges probed by our survey.

4 DISCUSSION

We studied the connection between low mass, star-forming galaxies and C IV absorbers at $z \approx 3.3$ using a sample of 86 Ly α emitting galaxies (LAEs). These LAEs are detected as part of the MUSEQuBES survey (Muzahid et al. 2020, 2021). Here we discuss our main findings described above.

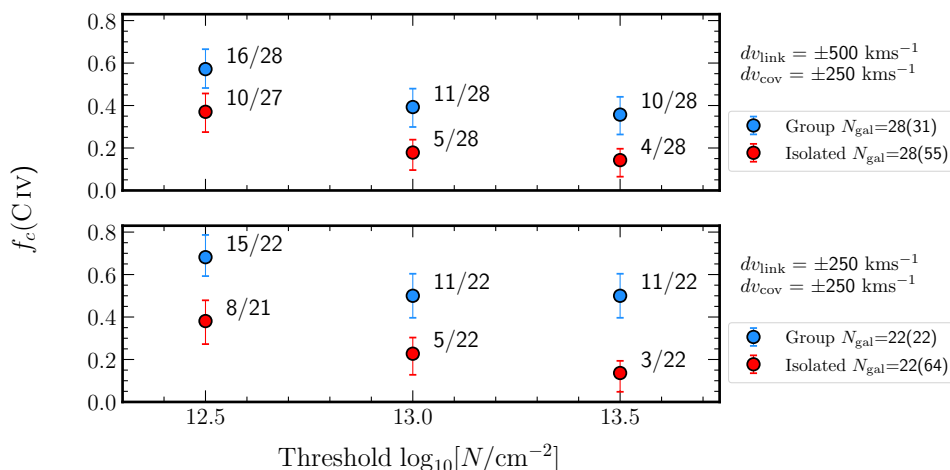


Figure 10. *Top:* Same as Fig 8 but for the “isolated” and “pair/group” LAEs separately. We defined a galaxy-pair/group in such a way that each member of a pair/group has at least one companion within $\pm 500 \text{ km s}^{-1}$ (dv_{link}) within the MUSE FoV. The impact parameters of the two subsamples are controlled so that for each threshold column density, the ρ distributions are indistinguishable. Here we used all the C IV absorbers within the LOS velocity window of $\pm 250 \text{ km s}^{-1}$ (dv_{cov}). The numbers next to the figure indicate the total number of pair/group or isolated LAEs in the controlled sample; the total number of pair/group LAEs is provided in parenthesis. “Pair/group” LAEs exhibit consistently higher covering fractions than the “isolated” ones. *Bottom:* Similar to the top, but for a dv_{link} of $\pm 250 \text{ km s}^{-1}$ instead of $\pm 500 \text{ km s}^{-1}$ for defining a pair/group. The environmental dependence appears to be stronger in this case.

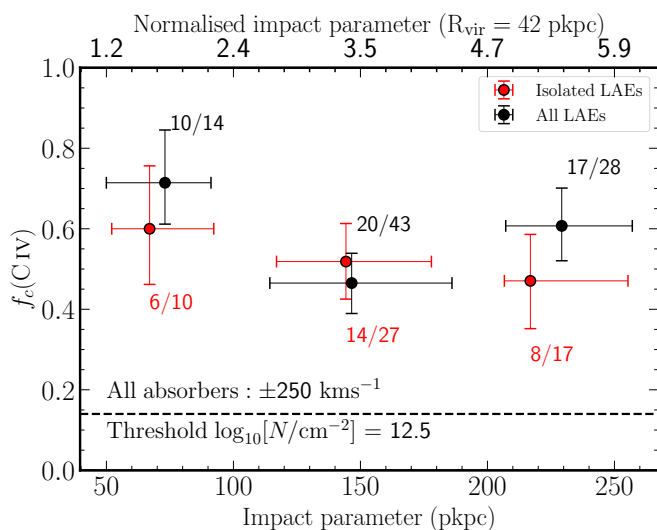


Figure 11. Covering fraction of C IV absorbers for the full LAE sample (in black) and for the isolated LAEs (in red) as a function of impact parameter, ρ . We split the sample into three impact parameter bins: 0–100 pkpc, 100–200 pkpc, and 200–320 pkpc. The top x-axis shows the normalized impact parameter where the normalization is done using the median $R_{\text{vir}} = 42 \text{ pkpc}$. The calculations are performed at a threshold $\log_{10} N/\text{cm}^{-2} = 12.5$ and using a LOS velocity window $\pm 250 \text{ km s}^{-1}$. The x-position of the dots reflects the median value in each impact parameter bin, while the error bar along the x-axis represents the 16 – 84 percentile range. The black dashed line is the covering fraction for the random sample at this particular threshold column density.

4.1 Connecting the LAEs and C IV absorbers

We cross-matched the blind C IV catalog with the LAE catalog and found an enhanced number of absorption components within $\pm 400 \text{ km s}^{-1}$ of the LAE redshifts, indicating a significant clustering between metal-enriched gas and low-mass,

star-forming galaxies at $z \approx 3.3$. A similar trend is seen for $z \approx 2.3$ LBGs and H I absorbers (Rudie et al. 2012). We further found that the higher column density C IV absorbers ($N > 10^{13} \text{ cm}^{-2}$) are more tightly correlated with the galaxies in velocity. Using the high resolution EAGLE cosmological simulation, Ho et al. (2021) recently showed that for low- z O VI gas selected via a velocity window of $\pm 500 \text{ km s}^{-1}$ (or $\pm 300 \text{ km s}^{-1}$) produces higher O VI column density than calculated within a fixed radius ($\approx 2\text{--}3 R_{\text{vir}}$) due to projection effects. The O VI covering fraction beyond $1 R_{\text{vir}}$ from $M_* \sim 10^9 M_{\odot}$ galaxies is dominated by absorbers located at 3D distances of more than $2 R_{\text{vir}}$. However, in order to be consistent with the previous studies in the literature we used a $\pm 500 \text{ km s}^{-1}$ velocity window for assigning absorption to a given galaxy (see e.g., Galbiati et al. 2023).

We found that 202 out of the 489 ‘blind’ C IV components lie within $\pm 500 \text{ km s}^{-1}$ of the LAE redshifts. The column density and Doppler parameter distributions of these 202 components are not significantly different from the remaining 287 components that are not associated with any LAEs (p -value of KS test being > 0.05). This could suggest two possibilities. First, the components with velocities $> 500 \text{ km s}^{-1}$ from any LAEs are likely associated with galaxies that are fainter in Ly α emission compared to the ones in our sample. Note that a fraction of LBGs does not show prominent Ly α emission (Kusakabe et al. 2020). However, from the LBG luminosity function presented in Steidel et al. (1999) we found that only ≈ 2 LBGs, brighter than I -band magnitude of 25, are expected to be present for the co-moving volume probed by our survey. On the other hand, those components can be related to low mass and/or low SFR galaxies that are below our detection threshold. Of course, a fraction of the components can be truly intergalactic in nature, though the metals must have been produced by stars inside galaxies.

The other possibility could be that not all the C IV components within $\pm 500 \text{ km s}^{-1}$ of the LAE redshifts are physically related to the LAEs themselves. To investigate this we

plotted the LOS velocity of all the C IV components within $\pm 500 \text{ km s}^{-1}$ of the LAE redshifts as a function of impact parameter and compared the LOS velocities to the escape velocity corresponding to the typical range in galaxy mass for our sample (see Fig. 5). Since the LOS velocity and impact parameter represent only lower limit on the actual 3D velocity and 3D distance from the galaxy, it is not straightforward to determine which components are actually bound to the galaxy from such a plot. However, the components outside the shaded regions in Fig. 5 are undoubtedly unbound to the galaxies. We found that 45% of the C IV components we associated with the LAEs (i.e. 91 out of 202) are not really bound to the LAEs. Earlier [Rudie et al. \(2019\)](#) also found that 5 out of 7 LBGs in their sample had some C IV components with LOS velocities greater than the corresponding escape velocity. This is in stark contrast to the studies at low- z relatively high-mass galaxies, where the majority of the CGM absorbers are bound to the host halos (e.g., [Tumlinson et al. 2011; Bordoloi et al. 2014; Werk et al. 2016](#)). However, there are certain instances of metal-rich gas with $v > v_{\text{esc}}$ that have been identified using highly ionized metal lines such as O VI (i.e., [Tripp 2011; Muzahid et al. 2015; Rosenwasser et al. 2018](#)).

We found that the median column density of the bound (unbound) components is $\log_{10} N/\text{cm}^{-2} = 12.8$ (12.7) and the median Doppler parameter is $b = 11.8$ (12.0) km s^{-1} . The column density and Doppler parameter distributions of the bound and unbound components do not seem to differ statistically, as suggested by KS-test results. In this context, recall that some fraction of the unbound components might not be related to the galaxies in question, but are associated with undetected lower-luminosity clustered galaxies. Fig. A.1 (Right) shows that the majority of the bound C IV components are within $\pm 250 \text{ km s}^{-1}$ of the LAE redshifts. The centroid of the best-fitting Gaussian ($-35.7 \pm 33.3 \text{ km s}^{-1}$) is consistent with the systemic redshift within 1.1σ allowed uncertainty.

4.2 The column density profile

We constructed the C IV column density profile (see Fig. 6) for the associated components (detected within $\pm 250 \text{ km s}^{-1}$ of an LAE). We found that the $N(\text{C IV})$ values associated with the LAEs are almost an order of magnitude higher compared to the mean $N(\text{C IV})$ estimated for the random sample. This indeed suggests that the associated components trace overdense regions with significant metal enrichment, likely the large-scale structures in which LAEs are embedded. However, we did not detect any statistically significant (anti) correlation between the C IV column density and impact parameter, at least not out to $\approx 250 \text{ pkpc}$. This is also true when only the bound absorbers are considered. This is consistent with [Muzahid et al. \(2021\)](#), but in contrast with some low- z surveys that reported an anti-correlation between the C IV column density and impact parameter (e.g., [Bordoloi et al. 2014; Liang & Chen 2014](#)). [Turner et al. \(2014\)](#) found a significant drop in the normalized C IV optical depth within R_{vir} , followed by a flat but still enhanced region beyond R_{vir} for LBGs. Because our LAEs are of lower mass (consequently lower R_{vir}) we may be probing the flat part of the radial profile. This warrants a larger sample size with impact parameters of $< R_{\text{vir}}$. A wider FoV of the future BlueMUSE,

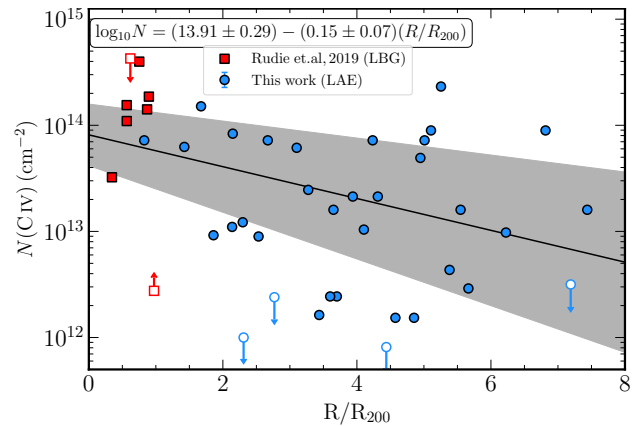


Figure 12. C IV column density profile compiled from the available literature. The filled squares (dots) represent C IV column density detections from [Rudie et al. \(2019\)](#) (this work), whereas the down-arrows (up-arrows) are the 3σ upper limits (lower limit) of the respective sample. The black solid line shows the model equation written on top of the figure. The best-fit parameters are estimated from the CENKEN function of NADA package (R) using only the high- z data points. The shaded region corresponds to the 1σ uncertainty of the fitted curve derived from the bootstrapped errors on the parameters.

on the other hand, can probe the large projected distances where the absorption signal asymptotically matches the IGM.

Similar to our finding, [Rudie et al. \(2019\)](#) also did not notice any significant trend between the total C IV column density, calculated within $\pm 1000 \text{ km s}^{-1}$ velocity window, and impact parameter ($< R_{\text{vir}}$) likely because of a smaller sample size of $8 \text{ } z \approx 2.3$ LBGs. The red squares in Fig. 12 represent their data points. The blue circles indicate the $N(\text{C IV})$ measurements within $\pm 1000 \text{ km s}^{-1}$ for the 35 MUSEQuBES LAEs for which we could estimate R_{vir} . Performing a Kendall- τ correlation test on this combined high- z sample (LBGs+LAEs), we found an anti-correlation between the total column density and impact parameter with $\tau_K = -0.2$ and $p\text{-value} = 0.03$, with a best-fit power-law relation: $N(\text{C IV}) = 10^{13.91 \pm 0.29} \text{ cm}^{-2} \times (R/R_{\text{vir}})^{-0.15 \pm 0.07}$.¹² The gray-shaded region corresponds to the 1σ uncertainty of this fitted curve derived using 1000 bootstrap realizations.

4.3 The covering fraction

Fig. 8 shows the measured C IV covering fractions for different threshold column densities. For a threshold column density of $10^{12.5} \text{ cm}^{-2}$, the C IV covering fraction of our sample is $\approx 64\%$, measured within a velocity window of $\pm 500 \text{ km s}^{-1}$. These f_c values are almost two times higher as compared to random regions. We did not find any significant dependence of f_c on either redshift or Ly α line luminosity in our sample. Similar to the column density profile, the covering fraction profile also does not show any appreciable anti-correlation with the impact parameter (see Fig. 11). This is also evident from Fig. 13 where we show the cumulative covering fraction

¹² We used the CENKEN function of NADA package in R which takes care of the upper limits. We excluded the only lower limit in the LBG sample from this exercise.

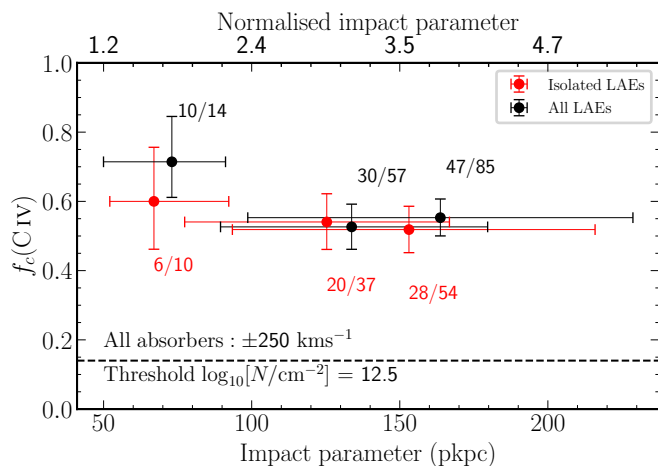


Figure 13. Cumulative covering fraction of all C IV absorbers within $\pm 250 \text{ km s}^{-1}$ of the LAEs as a function of impact parameter. The bin boundaries are chosen as 100, 200, and 320 pkpc. The rest is the same as in Fig. 11. With the impact parameter, the covering fraction around isolated LAEs reaches a value of $\approx 54\%$.

with impact parameter. The cumulative covering fraction remains constant for the impact parameter of $> 100 \text{ pkpc}$. A similar trend is also seen in the recent study by Galbiati et al. (2023), where the C IV covering fraction appears to reach a plateau at $\sim 100 - 250 \text{ pkpc}$ with a value very similar to ours (see their figure 10). The lack of any significant trend between C IV covering fraction and impact parameter in our sample owes to the fact that the largest impact parameter bin shows an equally high f_c value, particularly for the full sample, leading to an upturn in the profile. This upturn is less pronounced when we only consider the isolated LAEs. This suggests that the upturn is likely due to the environmental effects and that the covering fraction profile is flatter for the pair/group galaxies compared to the isolated ones.

We found a strong environmental dependence for $f_c(\text{C IV})$ (Fig. 10). Pair/group galaxies exhibit a higher C IV covering fraction compared to isolated galaxies. The difference in f_c increases when we consider a narrower linking velocity ($\pm 250 \text{ km s}^{-1}$) for defining pairs/groups. For example, at the threshold $\log_{10} N/\text{cm}^{-2} = 12.5$ (13.5), $f_c(\text{C IV})$ is $\approx 68\%$ (50%) for pair/group, whereas for isolated LAEs it is only $\approx 38\%$ (23%). Muzahid et al. (2021) reported a similar environmental dependence in which the pair/group LAEs showed a considerably stronger C IV absorption in the composite spectrum of background quasars. Recently, Galbiati et al. (2023) also showed that the covering fraction for their group LAEs was almost three times stronger than that for the isolated ones. They calculated a C IV covering fraction of $\approx 60\%$ within $\sim 200 \text{ pkpc}$ their group galaxies and $\approx 20\%$ around isolated LAEs. Our finding is consistent with both results. The enhanced C IV covering fraction around pair/group galaxies suggests that (a) they live in significantly more metal-rich environments and/or (b) their surroundings ensure favorable ionization conditions for the triply ionized carbon and/or (c) the gas density or the number density of the clouds are higher for them. To understand this better, in future works we will explore this environmental dependence for other low- and intermediate-ionization state lines such as

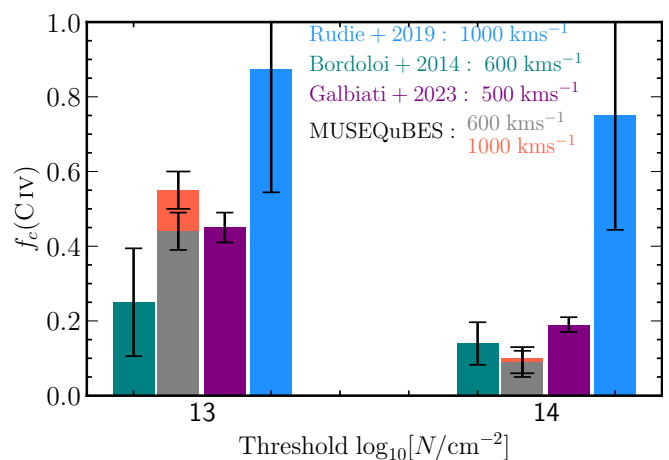


Figure 14. A comparison between the C IV covering fraction of high- z ($35 < \rho/\text{pkpc} < 100$) LBGs from Rudie et al. (2019, blue bar), low- z ($14 < \rho/\text{pkpc} < 135$) dwarf galaxies from Bordoloi et al. (2014, teal bar), and $z \approx 3.3$ LAEs Galbiati et al. (2023, purple bar) with our high- z MUSEQuBES sample ($16 < \rho/\text{pkpc} < 315$) at two different threshold column densities. The impact parameter range for Galbiati et al. (2023) is similar to us. The legend includes the velocity window that was used in respective surveys to calculate f_c . To compare these findings with our results, we also estimated the f_c within ± 1000 (orange bar) and $\pm 600 \text{ km s}^{-1}$ (grey bar) of MUSEQuBES LAEs. While f_c is calculated within the virial radii of the LBGs and low- z dwarfs, the median impact parameter for both Galbiati et al. (2023) and our sample is several times the virial radius.

Si II, Si III, and Si IV. The highly ionized O VI lines are unfortunately too severely blended with the LAF.

In Fig. 14 we compared our f_c measurements with that of Rudie et al. (2019), Galbiati et al. (2023) and Bordoloi et al. (2014). The sample of Rudie et al. (2019) contains only a handful of $z \approx 2.3$ LBGs within $35 < \rho/\text{pkpc} < 100$, whereas the sample of Bordoloi et al. (2014) contains about 40 $z < 0.1$ dwarf galaxies within $14 < \rho/\text{pkpc} < 135$. Both the redshift ($3 < z < 4.5$) and impact parameter range covered by Galbiati et al. (2023) is very similar to us. They provided C IV covering fractions at different threshold equivalent widths, but for the sake of comparison, we converted them to column densities using the linear part of the COG relation. To be consistent with the velocity windows used to calculate the covering fractions in these studies, we recalculated the covering fractions for our MUSEQuBES galaxies¹³. It is evident from the figure that high column density C IV absorbers ($N(\text{C IV}) > 10^{14} \text{ cm}^{-2}$) are more frequently detected around the $z \approx 2.3$ LBGs compared to the $z \approx 3 - 4$ LAEs and $z < 0.1$ dwarf galaxies. The difference in C IV covering fraction around LBGs and LAEs are not significant for a lower threshold column density of 10^{13} cm^{-2} . We point out here that the quasar sightlines are always passing within the virial radii for the LBGs and low- z dwarfs, whereas the median impact parameter of the high- z LAEs is several times the virial radius. Finally, for the lower $N(\text{C IV})$ threshold of 10^{13} cm^{-2} our f_c value is fully consistent with Galbiati et al. (2023). We confirmed that the marginal difference in f_c values seen for

¹³ The f_c values for MUSEQuBES sample at $dv = \pm 500 \text{ km s}^{-1}$ and 600 km s^{-1} are identical.

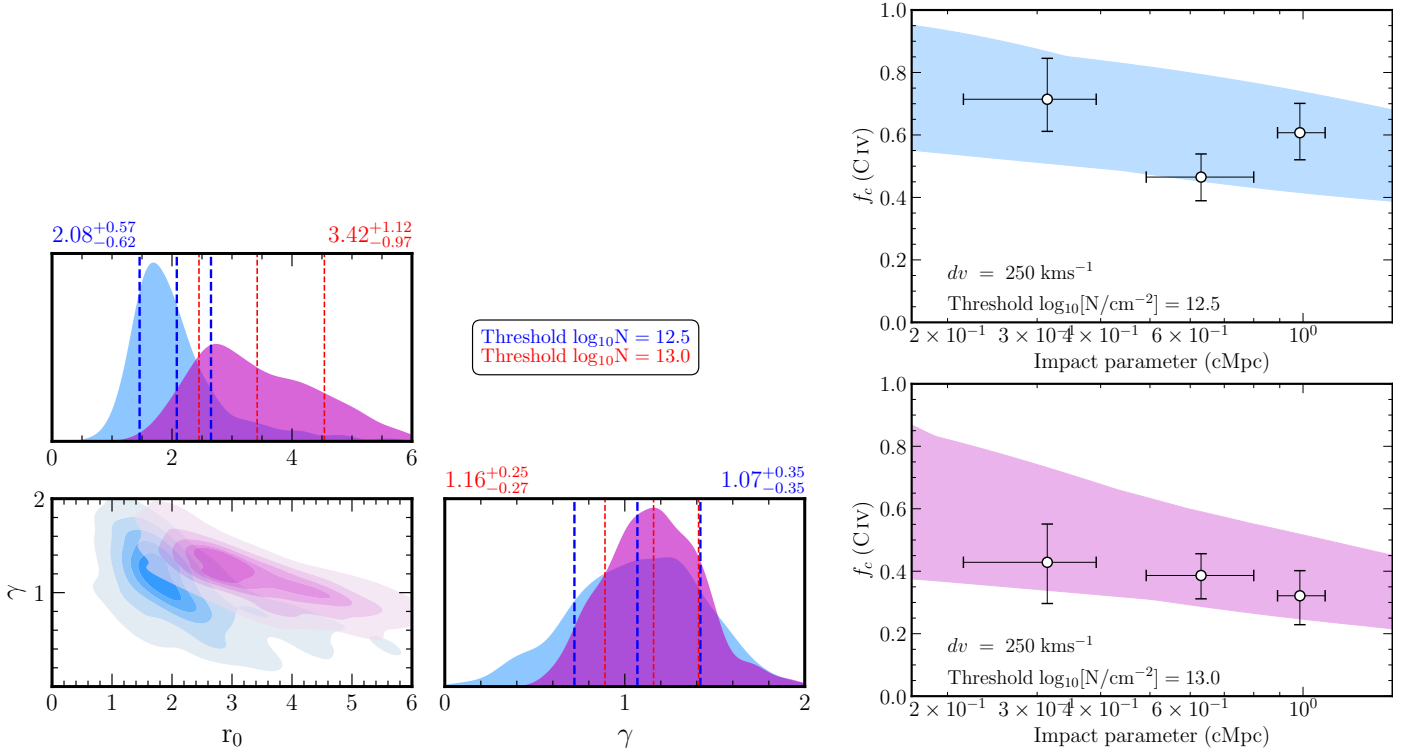


Figure 15. *Left:* The corner plot showing the posterior distribution of parameters r_0 and γ of the galaxy-absorber cross-correlation function (ξ_{ga}) along with their 2D density plot for two different threshold C IV column densities as indicated by the legend. Here, only the C IV absorbers within $\pm 250 \text{ km s}^{-1}$ of the LAEs are used. Vertical dashed lines indicate the 16–50–84 percentile range of the respective distributions. These values are also mentioned at the top of the density plots. Though the γ values are very similar, it should be noted that the r_0 value is larger for higher threshold column density. For threshold column density $\log_{10} N/\text{cm}^{-2} = 12.5$, $r_0 = 2.08 h^{-1} \text{ cMpc}$ and for $\log_{10} N/\text{cm}^{-2} = 13.0$, it is $r_0 = 3.42 h^{-1} \text{ cMpc}$ ($h = 0.7$). *Right-top:* Covering fraction of C IV as a function of impact parameter for a threshold column density of $\log_{10} N/\text{cm}^{-2} = 12.5$ and LOS velocity window $= \pm 250 \text{ km s}^{-1}$ (binning and error bars are same as in Fig. 11). The (blue) band showing the covering fraction profile corresponding to the r_0 and γ values drawn from the 99% confidence level of their respective posterior sample space. *Right-bottom:* Same as the top but for a threshold column density of $\log_{10} N/\text{cm}^{-2} = 13.0$.

the higher threshold column density is due to the fact that 0.3 \AA threshold used in Galbiati et al. (2023) corresponds to $N(\text{C IV})$ of $10^{13.87} \text{ cm}^{-2}$ in the linear part of the COG.

4.4 Galaxy-absorber 2-point correlation function

We found that the C IV column densities and covering fractions are significantly enhanced near the LAE redshifts compared to random regions, indicating a strong spatial correlation between the LAEs and C IV absorbers. In this section we will put constraints on the LAE and C IV absorber cross-correlation function using the covering fraction profile following Wilde et al. (2021) (see also Hennawi & Prochaska 2007). The absorber-galaxy clustering can be defined as the excess number of absorbers around galaxies with respect to random regions, i.e.,

$$\chi = \frac{N_{\text{obs}} - N_{\text{rand}}}{N_{\text{rand}}},$$

where, $N_{\text{rand}} (= \langle \frac{dN}{dz} \rangle \delta z)$ is the average number of absorbers above a threshold column density within a velocity window of $\delta z = (1+z) \frac{2\delta v}{c}$. N_{obs} is the observed number of absorbers. We will adopt the standard parametrization for the galaxy-

absorber correlation function,

$$\xi_{ga}(r) = \left(\frac{r}{r_0} \right)^{-\gamma},$$

where r ($\equiv \sqrt{r_{\perp}^2 + r_{\parallel}^2}$) is the 3D distance between the galaxy and the absorber. Here, r_{\parallel} is estimated using pure Hubble flow and then converted to comoving scale. This ξ_{ga} is related to the galaxy-absorber 3D cross-correlation function:

$$\chi(r) = \frac{1}{V} \int_V \xi_{ga} dV.$$

Say that out of \mathcal{N} quasar-galaxy pairs, \mathcal{N}' exhibit C IV absorption with total column density above a threshold value ($N_{\text{C IV}}$) within a velocity window of $2\delta v$, then one can estimate the parameters r_0 and γ using the following likelihood function:

$$\mathcal{L} = \prod_{i=0}^{\mathcal{N}'} P_i^{\text{hit}}(r) \prod_{j=0}^{\mathcal{N}-\mathcal{N}'} P_j^{\text{miss}}(r),$$

where, P_{hit} (P_{miss}) is the probability of detecting (not detecting) a C IV absorber within $\pm \delta v$ of the galaxies. The probability of non-detection can also be expressed as a Poissonian distribution of zero events and a rate of N_{obs} , i.e.,

$$P^{\text{miss}}(r) = \exp \left[-\{1 - \chi(r)\} \left\langle \frac{dN}{dz} \right\rangle \delta z \right],$$

and $P^{\text{hit}}(r) = 1 - P^{\text{miss}}(r)$. Note that P^{hit} is nothing but the covering fraction (f_c).

For our sample, $\langle \frac{dN}{dz} \rangle$ for a threshold column density of $\log_{10} N/\text{cm}^{-2} = 12.5$ (13) is ≈ 55 (22) and $\delta v = 250 \text{ km s}^{-1}$. In order to estimate the parameters, we have followed a Bayesian approach. Our priors are defined such that r_0 obeys a flat prior that ranges between 0 and $6 h^{-1} \text{ cMpc}$ ($h = 0.7$) and γ follow a Gaussian prior with $\mu = 1.6$ and $\sigma = 0.5$ (provided, $\gamma > 0$). These priors were chosen based on the results from the literature (see Wilde et al. 2021; Adelberger et al. 2005). Using the ULTRANEST package of PYTHON, we estimated the posterior distributions of the parameters. Fig. 15 (left) shows the corner plots of the parameters for two different threshold column densities. The right panel of Fig. 15 shows the covering fraction profiles for two threshold column densities corresponding to the posterior distributions of both parameters. Our observed data points are plotted on top (white circles) with respective 1σ binomial confidence limits. For the threshold $\log_{10} N/\text{cm}^{-2} = 12.5$, we obtained $r_0 = 2.1 h^{-1} \text{ cMpc} \equiv 338.6 \text{ pkpc}$ and power-law slope, $\gamma = 1.1$. Similarly, for the threshold $\log_{10} N/\text{cm}^{-2} = 13.0$, $r_0 = 3.4 h^{-1} \text{ cMpc} \equiv 556.7 \text{ pkpc}$ and $\gamma = 1.2$. The fact that r_0 increases for a higher threshold column density is consistent with the findings of Adelberger et al. (2005). The r_0 value for our LAE sample and high column density ($\log_{10} N/\text{cm}^{-2} = 13.0$) C IV absorber correlation function agrees well with their galaxy-galaxy correlation length scales (see also Herrero Alonso et al. (2021)), supporting that the high column density C IV absorbers are effective tracers of galaxy halos.

5 CONCLUSIONS

This work is a continuation of the MUSEQuBES survey at high- z (Muzahid et al. 2021), which focuses on the CGM of high- z ($3 < z < 4$) LAEs. MUSEQuBES presented a sample of 96 LAEs in the redshift range 2.9–3.8, detected in 8 MUSE fields centered on 8 bright background quasars. The VLT/UVES and/or Keck/HIRES spectra of these 8 quasars allow us to probe the C IV absorption from the CGM of 86 of the 96 MUSEQuBES galaxies.

To carry out an unbiased study, we first prepared a “blind” catalog of C IV absorbers irrespective of the LAEs. We searched for the C IV $\lambda\lambda 1548, 1550$ doublet in the 8 high resolution ($\text{FWHM} \approx 6.6 \text{ km s}^{-1}$), high SNR (> 30 per pixel) quasar spectra visually using the doublet matching technique. Voigt profile decomposition of all the detected C IV absorbers gave rise to a total of 489 C IV absorption components in the redshift range 2.9–3.8, with column densities ranging from $10^{11.4}$ to $10^{14.3} \text{ cm}^{-2}$ (median $10^{12.7} \text{ cm}^{-2}$) and Doppler parameter in the range $0.87 - 41.4 \text{ km s}^{-1}$ (median $= 12.0 \text{ km s}^{-1}$). The CDDF constructed out of these C IV components has a power-law slope of -2.12 ± 0.11 , which is consistent with the values obtained in the literature at similar redshifts with larger sample sizes. Next, we crossed-matched the ‘blind’ C IV absorber catalog and the LAE catalog to investigate the relation(s) between them. Our main findings are as follows:

- There is an enhancement of C IV absorbers within $\pm 400 \text{ km s}^{-1}$ of the LAEs (Fig. 4). The high column density absorbers ($\log_{10} N/\text{cm}^{-2} > 13.0$) are more tightly bound

to the LAEs (within $\pm 320 \text{ km s}^{-1}$, Fig. A.1: left). To be consistent with the existing literature, we adopted a velocity window of $\pm 500 \text{ km s}^{-1}$ for associating the LAEs and absorbers.

- We found only $\approx 55\%$ of these associated absorbers are bound to the LAEs, i.e., they are falling within the escape velocity range of these LAEs (Fig. 5). These bound absorbers are more tightly correlated to the LAEs in velocity (i.e., within $\pm 250 \text{ km s}^{-1}$, Fig. A.1: right).

- We did not find any significant correlation between the total C IV column density of the absorbers associated with the LAEs and the impact parameter in the range $16 \leq \rho \leq 315 \text{ pkpc}$ using either non-parametric or parametric methods. The observed column densities are, however, considerably higher compared to random regions (Fig. 6).

- We did not find any significant trend between the Doppler parameter of the associated C IV components and ρ (Fig. 7). The $b(\text{C IV})$ distributions of the associated components and the rest are statistically indistinguishable.

- We found that the C IV covering fractions around the LAEs, averaged over the complete impact parameter range of our sample at different threshold column densities, are ≈ 2 times larger compared to random regions (Fig. 8).

- We did not see any redshift evolution of the C IV covering fraction in our sample (Fig. 9).

- The C IV covering fraction is ≈ 2 times higher for the pair/group sample compared to the isolated ones (Fig. 10).

- The C IV covering fraction does not vary much with the impact parameter within $16 \leq \rho \leq 315 \text{ pkpc}$. For the isolated LAEs, even at the farthest impact parameter bin (i.e., $\approx 200 - 250 \text{ pkpc}$), we found a covering fraction of 0.5 ± 0.1 for a threshold $\log_{10} N/\text{cm}^{-2} = 12.5$, which is nearly three times more compared to random regions (Fig. 11).

- Finally, we estimated the best-fit parameters of the LAE-C IV absorber cross-correlation function using the C IV covering fraction profile. We obtained a scale-length, r_0 of $= 2.1 h^{-1} \text{ cMpc}$ ($3.4 h^{-1} \text{ cMpc}$) and a power-law slope, γ of 1.1 (1.2) for a threshold column density $\log_{10} N/\text{cm}^{-2} = 12.5$ (13.5) (Fig. 15).

This is the third paper that presents results from the MUSEQuBES high- z survey. In the future, we intend to present the connection between H I and other metal lines associated with these LAEs along these 8 sightlines and determine the physical properties of the CGM surrounding these LAEs in greater detail.

DATA AVAILABILITY

The data underlying this article are available in ESO (<http://archive.eso.org/cms.html>) and Keck (<https://www2.keck.hawaii.edu/koa/public/koa.php>) public archives.

ACKNOWLEDGEMENT

This paper uses the following software: NumPy (Harris et al. 2020), SciPy (Virtanen et al. 2020), Matplotlib (Hunter 2007), and AstroPy (Astropy Collaboration et al. 2013, 2018).

EB thanks Labanya Kumar Guha and Sapna Mishra for helpful discussions. EB and SM thank Raghunathan Srianand for useful discussion.

REFERENCES

- Adelberger K. L., Steidel C. C., Shapley A. E., Pettini M., 2003, *ApJ*, **584**, 45
- Adelberger K. L., Shapley A. E., Steidel C. C., Pettini M., Erb D. K., Reddy N. A., 2005, *The Astrophysical Journal*, **629**, 636
- Astropy Collaboration et al., 2013, *A&A*, **558**, A33
- Astropy Collaboration et al., 2018, *AJ*, **156**, 123
- Bacon R., et al., 2010, in McLean I. S., Ramsay S. K., Takami H., eds, *Society of Photo-Optical Instrumentation Engineers (SPIE) Conference Series Vol. 7735, Ground-based and Airborne Instrumentation for Astronomy III*. p. 773508 ([arXiv:2211.16795](https://arxiv.org/abs/2211.16795)), doi:10.1117/12.856027
- Behroozi P., Wechsler R. H., Hearin A. P., Conroy C., 2019, *MNRAS*, **488**, 3143
- Bordoloi R., et al., 2014, *ApJ*, **796**, 136
- Borisova E., et al., 2016, *ApJ*, **831**, 39
- Borthakur S., Heckman T., Strickland D., Wild V., Schiminovich D., 2013, *The Astrophysical Journal*, **768**, 18
- Buchner J., 2014, [arXiv e-prints](https://arxiv.org/abs/1407.5459), p. [arXiv:1407.5459](https://arxiv.org/abs/1407.5459)
- Buchner J., 2019, *PASP*, **131**, 108005
- Buchner J., 2021, *The Journal of Open Source Software*, **6**, 3001
- Burchett J. N., et al., 2016, *The Astrophysical Journal*, **832**, 124
- Cantalupo S., Arrigoni-Battaia F., Prochaska J. X., Hennawi J. F., Madau P., 2014, *Nature*, **506**, 63
- Cantalupo S., et al., 2018, *Monthly Notices of the Royal Astronomical Society*, **483**, 5188
- Carswell R. F., Webb J. K., 2014, VPFIT: Voigt profile fitting program, Astrophysics Source Code Library, record ascl:1408.015 ([ascl:1408.015](https://arxiv.org/abs/1408.015))
- Chabrier G., 2003, *PASP*, **115**, 763
- Chen H. W., Lanzetta K. M., Webb J. K., Barcons X., Fernández-Soto A., 1998, [arXiv e-prints](https://arxiv.org/abs/ppastro-ph/9809297), [pp astro-ph/9809297](https://arxiv.org/abs/ppastro-ph/9809297)
- Chen H.-W., Lanzetta K. M., Webb J. K., 2001, *The Astrophysical Journal*, **556**, 158
- Chen H.-W., Helsby J. E., Gauthier J.-R., Shectman S. A., Thompson I. B., Tinker J. L., 2010, *ApJ*, **714**, 1521
- D’Odorico V., Calura F., Cristiani S., Viel M., 2010, *MNRAS*, **401**, 2715
- Dutta R., et al., 2023a, [arXiv e-prints](https://arxiv.org/abs/2302.09087), p. [arXiv:2302.09087](https://arxiv.org/abs/2302.09087)
- Dutta S., Muzahid S., Schaye J., Mishra S., Chen H.-W., Johnson S., Wisotzki L., Cantalupo S., 2023b, [arXiv e-prints](https://arxiv.org/abs/2303.16933), p. [arXiv:2303.16933](https://arxiv.org/abs/2303.16933)
- Ellison S. L., Songaila A., Schaye J., Pettini M., 2000, *AJ*, **120**, 1175
- Galbiati M., Fumagalli M., Fossati M., Lofthouse E. K., Dutta R., Prochaska J. X., Murphy M. T., Cantalupo S., 2023, [arXiv e-prints](https://arxiv.org/abs/2302.00021), p. [arXiv:2302.00021](https://arxiv.org/abs/2302.00021)
- Harris C. R., et al., 2020, *Nature*, **585**, 357
- Hellsten U., Hernquist L., Katz N., Weinberg D. H., 1998, *ApJ*, **499**, 172
- Hennawi J. F., Prochaska J. X., 2007, *ApJ*, **655**, 735
- Herrero Alonso Y., et al., 2021, *A&A*, **653**, A136
- Ho S. H., Martin C. L., Schaye J., 2021, *ApJ*, **923**, 137
- Hunter J. D., 2007, *Computing in Science and Engineering*, **9**, 90
- Johnson S. D., Chen H.-W., Mulchaey J. S., Schaye J., Straka L. A., 2017, *ApJ*, **850**, L10
- Johnson S. D., et al., 2022, [arXiv e-prints](https://arxiv.org/abs/2209.04245), p. [arXiv:2209.04245](https://arxiv.org/abs/2209.04245)
- Kelly B. C., 2007, *ApJ*, **665**, 1489
- Kennicutt Robert C. J., 1998, *ARA&A*, **36**, 189
- Kusakabe H., et al., 2020, *A&A*, **638**, A12
- Liang C. J., Chen H.-W., 2014, *Monthly Notices of the Royal Astronomical Society*, **445**, 2061
- Lofthouse E. K., et al., 2023, *MNRAS*, **518**, 305
- Madau P., Dickinson M., 2014, *ARA&A*, **52**, 415
- McGaugh S. S., Schombert J. M., de Blok W. J. G., Zagursky M. J., 2010, *ApJ*, **708**, L14
- Morrissey P., et al., 2018, *The Astrophysical Journal*, **864**, 93
- Moster B. P., Naab T., White S. D. M., 2013, *MNRAS*, **428**, 3121
- Muzahid S., Srianand R., Bergeron J., Petitjean P., 2012, *MNRAS*, **421**, 446
- Muzahid S., Kacprzak G. G., Churchill C. W., Charlton J. C., Nielsen N. M., Mathes N. L., Trujillo-Gomez S., 2015, *ApJ*, **811**, 132
- Muzahid S., et al., 2020, *MNRAS*, **496**, 1013
- Muzahid S., et al., 2021, *MNRAS*, **508**, 5612
- Nielsen N. M., Churchill C. W., Kacprzak G. G., 2013, *ApJ*, **776**, 115
- Peeples M. S., Werk J. K., Tumlinson J., Oppenheimer B. D., Prochaska J. X., Katz N., Weinberg D. H., 2014, *The Astrophysical Journal*, **786**, 54
- Péroux C., Rahmani H., Arrigoni Battaia F., Augustin R., 2018, *MNRAS*, **479**, L50
- Rakic O., Schaye J., Steidel C. C., Rudie G. C., 2012, *The Astrophysical Journal*, **751**, 94
- Rosenwasser B., Muzahid S., Charlton J. C., Kacprzak G. G., Wakker B. P., Churchill C. W., 2018, *MNRAS*, **476**, 2258
- Rubin K. H. R., Diamond-Stanic A. M., Coil A. L., Crighton N. H. M., Moustakas J., 2018, *ApJ*, **853**, 95
- Rudie G. C., et al., 2012, *The Astrophysical Journal*, **750**, 67
- Rudie G. C., Steidel C. C., Pettini M., Trainor R. F., Strom A. L., Hummels C. B., Reddy N. A., Shapley A. E., 2019, *The Astrophysical Journal*, **885**, 61
- Schaye J., Aguirre A., Kim T.-S., Theuns T., Rauch M., Sargent W. L. W., 2003, *ApJ*, **596**, 768
- Schroetter I., et al., 2021, *MNRAS*, **506**, 1355
- Songaila A., 2001, *ApJ*, **561**, L153
- Steidel C. C., Adelberger K. L., Gialalisco M., Dickinson M., Pettini M., 1999, *ApJ*, **519**, 1
- Steidel C. C., Erb D. K., Shapley A. E., Pettini M., Reddy N., Bogosavljević M., Rudie G. C., Rakic O., 2010, *The Astrophysical Journal*, **717**, 289
- Tripp T., 2011, in *American Astronomical Society Meeting Abstracts #217*. p. 102.01
- Tumlinson J., et al., 2011, *The Astrophysical Journal*, **733**, 111
- Tumlinson J., Peeples M., Werk J., 2017, *Annual Review of Astronomy and Astrophysics*, **55**
- Turner M. L., Schaye J., Steidel C. C., Rudie G. C., Strom A. L., 2014, *MNRAS*, **445**, 794
- Verhamme A., Schaerer D., Maselli A., 2006, *A&A*, **460**, 397
- Virtanen P., et al., 2020, *Nature Methods*, **17**, 261
- Werk J. K., et al., 2014, *ApJ*, **792**, 8
- Werk J. K., et al., 2016, *ApJ*, **833**, 54
- Wilde M. C., et al., 2021, *ApJ*, **912**, 9
- Wisotzki L., et al., 2018, *Nature*, **563**, E31
- Zabl J., et al., 2021, *MNRAS*, **507**, 4294

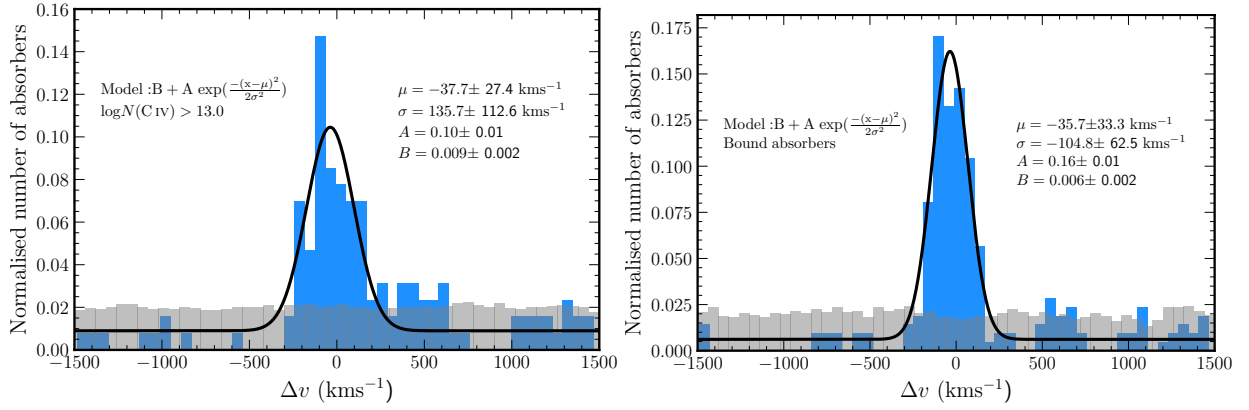


Figure A.1. *Left:* Same as Fig. 4 but for the high column density ($\log_{10} N/\text{cm}^{-2} > 13.0$) absorbers only. The σ is smaller in this case than the complete sample implying that the high column density absorbers are more tightly related to the LAEs. *Right:* Same as the **left** but only for the “bound” absorbers. Note that some absorbers that are bound to some LAEs ($< \pm 500 \text{ km s}^{-1}$) can be at some large velocities w.r.t. other LAEs of the same sightline. The best-fitted parameters of the model suggest an enhancement of C IV absorption within $\pm 105 \text{ km s}^{-1}$ corresponding to an FWHM of $\approx 247 \text{ km s}^{-1}$.

APPENDIX A:

This Appendix contains Fig. A.1 and an “online only” Table A1. Fig. A.1 shows the redshift distribution of the high-column density ($\log_{10} N/\text{cm}^{-2} > 13.0$) C IV absorbers on the **Left** and of bound C IV absorbers on the **Right** with respect to the LAEs (see section 3.2 for details). Table A1 presents the best-fit parameters of Voigt profiles fitted to blindly searched C IV components.

Table A1: The “blind” C IV absorber catalog

Index	Qso Name	z	z -error	b (km s ⁻¹)	b -error (km s ⁻¹)	$\log_{10} N/\text{cm}^{-2}$	$\log_{10} N/\text{cm}^{-2}$ -error
0	Q1422+23	2.916950	0.000010	8.42	0.66	12.82	0.02
1	Q1422+23	2.959160	0.000010	21.14	0.83	13.43	0.02
2	Q1422+23	2.959610	0.000010	12.43	0.95	13.11	0.03
3	Q1422+23	2.960040	0.000000	11.47	0.57	13.38	0.02
4	Q1422+23	2.960320	0.000010	6.76	1.26	12.73	0.08
5	Q1422+23	2.960590	0.000020	11.93	3.02	12.58	0.09
6	Q1422+23	2.960970	0.000000	7.63	0.50	12.90	0.02
7	Q1422+23	2.982490	0.000010	11.71	1.65	12.43	0.05
8	Q1422+23	3.018530	0.000010	15.72	1.60	12.75	0.04
9	Q1422+23	3.037290	0.000010	10.63	0.68	12.99	0.02
10	Q1422+23	3.246490	0.000010	9.11	1.46	12.63	0.05
11	Q1422+23	3.281060	0.000050	19.42	3.43	13.13	0.09
12	Q1422+23	3.281430	0.000020	11.76	2.73	12.94	0.14
13	Q1422+23	3.288810	0.000030	17.37	3.17	12.70	0.06
14	Q1422+23	3.329950	0.000010	7.60	1.37	12.36	0.05
15	Q1422+23	3.330330	0.000010	11.72	1.51	12.57	0.04

16	Q1422+23	3.388730	0.000150	13.00	5.14	12.71	0.66
17	Q1422+23	3.389010	0.000060	15.04	5.59	13.22	0.28
18	Q1422+23	3.389460	0.000120	19.60	9.64	12.76	0.27
19	Q1422+23	3.417110	0.000010	10.36	1.33	12.60	0.04
20	Q1422+23	3.423080	0.000020	25.77	2.30	12.84	0.03
21	Q1422+23	3.428230	0.000010	6.44	0.88	12.60	0.04
22	Q1422+23	3.482100	0.000010	24.33	1.03	13.72	0.02
23	Q1422+23	3.500490	0.000020	12.89	2.69	12.79	0.06
24	Q1422+23	3.547890	0.000010	13.66	0.69	13.61	0.02
25	Q1422+23	3.548330	0.000020	13.16	1.62	13.00	0.05
26	Q1422+23	3.565630	0.000020	16.07	2.11	12.66	0.04
27	Q1422+23	3.576250	0.000020	3.40	2.36	12.27	0.13
28	Q1422+23	3.576620	0.000010	15.67	1.35	13.27	0.03
29	Q1422+23	3.577180	0.000010	13.10	1.35	13.19	0.04
30	Q1422+23	3.577640	0.000010	11.86	0.63	13.34	0.02
31	Q1422+23	3.602830	0.000020	6.38	1.77	12.42	0.07
32	Q1422+23	3.603220	0.000010	9.06	0.64	13.26	0.02
33	Q1422+23	3.603520	0.000020	6.28	2.05	12.69	0.16
34	Q1422+23	3.603800	0.000040	12.63	4.07	12.78	0.13
35	Q1422+23	3.604470	0.000010	17.12	0.97	13.30	0.02
36	Q1422+23	3.605420	0.000020	25.21	1.62	13.61	0.03
37	Q1422+23	3.606060	0.000010	16.05	0.54	13.91	0.01
38	Q1422+23	3.606500	0.000010	5.88	1.50	12.61	0.09
39	Q1422+23	3.606840	0.000010	5.46	1.14	12.73	0.07
40	Q1422+23	3.606900	0.000000	30.68	2.64	13.32	0.03
41	Q1422+23	3.608330	0.000030	27.43	2.69	12.89	0.04
42	Q1422+23	3.609440	0.000000	11.35	0.44	13.23	0.01
43	Q1422+23	3.609850	0.000010	5.93	0.92	12.58	0.04
44	Q1422+23	3.742420	0.000020	15.72	1.52	13.19	0.03
45	Q1422+23	3.756060	0.000260	41.45	10.91	13.46	0.23
46	Q1422+23	3.756830	0.000080	31.20	7.04	13.56	0.21
47	Q1422+23	3.757670	0.000050	23.79	2.97	13.28	0.08
48	Q1422+23	3.758950	0.000030	29.25	2.72	13.31	0.04
49	Q1422+23	3.759410	0.000010	6.77	1.12	12.85	0.07

50	Q1422+23	3.760410	0.000010	12.97	0.61	13.31	0.02
51	Q1422+23	3.760000	0.000000	4.97	1.41	12.52	0.07
52	Q1422+23	3.770610	0.000020	9.75	1.67	12.69	0.06
53	Q1422+23	3.792550	0.000020	14.10	1.60	12.76	0.04
54	Q1422+23	3.812220	0.000010	12.75	1.42	12.81	0.05
55	Q1422+23	3.813650	0.000000	5.65	0.13	13.92	0.02
56	Q1422+23	3.814170	0.000020	1.45	4.88	12.19	0.15
57	Q1422+23	3.834550	0.000040	30.55	3.27	13.20	0.04
58	Q1422+23	3.835090	0.000020	6.54	2.26	12.50	0.14
59	Q1317-0507	2.908860	0.000020	10.16	1.34	12.90	0.09
60	Q1317-0507	2.909050	0.000000	3.44	0.89	12.90	0.15
61	Q1317-0507	2.909200	0.000030	12.23	8.67	13.01	0.28
62	Q1317-0507	2.909500	0.000000	10.87	0.81	13.12	0.02
63	Q1317-0507	2.909530	0.000000	5.79	0.34	13.03	0.03
64	Q1317-0507	2.911400	0.000000	6.72	0.06	13.56	0.00
65	Q1317-0507	2.942030	0.000000	7.02	0.52	12.56	0.04
66	Q1317-0507	2.942120	0.000020	22.01	1.96	12.55	0.05
67	Q1317-0507	2.984870	0.000010	14.66	0.96	12.69	0.02
68	Q1317-0507	2.986390	0.000000	2.30	0.45	13.49	0.12
69	Q1317-0507	2.986620	0.000000	17.54	0.20	14.35	0.01
70	Q1317-0507	2.987070	0.000000	9.59	0.56	13.39	0.02
71	Q1317-0507	2.987460	0.000010	14.06	1.41	13.32	0.04
72	Q1317-0507	2.987670	0.000010	4.13	2.08	12.39	0.22
73	Q1317-0507	2.988220	0.000000	9.32	0.36	13.03	0.02
74	Q1317-0507	2.988810	0.000050	36.95	5.14	13.05	0.05
75	Q1317-0507	2.988950	0.000010	13.23	1.79	12.67	0.12
76	Q1317-0507	2.989570	0.000010	12.59	0.90	12.66	0.04
77	Q1317-0507	3.064590	0.000000	8.80	0.74	12.82	0.03
78	Q1317-0507	3.065050	0.000000	17.88	0.26	14.01	0.00
79	Q1317-0507	3.065430	0.000000	9.12	0.36	13.22	0.02
80	Q1317-0507	3.065780	0.000010	17.50	2.89	12.83	0.06
81	Q1317-0507	3.066100	0.000010	10.10	1.46	12.65	0.07
82	Q1317-0507	3.066410	0.000010	11.39	1.44	13.05	0.08
83	Q1317-0507	3.066680	0.000020	13.62	1.21	13.09	0.06

84	Q1317-0507	3.076320	0.000000	5.11	0.74	12.49	0.06
85	Q1317-0507	3.076480	0.000020	27.79	1.90	13.20	0.03
86	Q1317-0507	3.076910	0.000010	5.17	0.00	12.67	0.03
87	Q1317-0507	3.077240	0.000000	19.23	2.41	13.13	0.04
88	Q1317-0507	3.077610	0.000020	10.61	0.00	12.64	0.05
89	Q1317-0507	3.077960	0.000030	10.95	4.53	12.64	0.09
90	Q1317-0507	3.078380	0.000010	8.51	0.83	12.63	0.04
91	Q1317-0507	3.078760	0.000010	10.48	0.86	12.70	0.02
92	Q1317-0507	3.098030	0.000040	11.64	0.00	12.15	0.10
93	Q1317-0507	3.098380	0.000020	14.35	3.31	12.57	0.08
94	Q1317-0507	3.098760	0.000020	11.35	1.87	12.44	0.07
95	Q1317-0507	3.148170	0.000010	15.32	0.73	12.83	0.02
96	Q1317-0507	3.148640	0.000020	13.32	2.06	12.27	0.06
97	Q1317-0507	3.187630	0.000000	10.23	1.64	12.32	0.06
98	Q1317-0507	3.187940	0.000000	11.13	1.10	12.61	0.05
99	Q1317-0507	3.188100	0.000000	13.84	0.83	12.72	0.03
100	Q1317-0507	3.306710	0.000010	6.55	1.18	12.16	0.08
101	Q1317-0507	3.307090	0.000050	19.85	7.34	12.14	0.12
102	Q1317-0507	3.389970	0.000010	4.80	1.04	11.91	0.05
103	Q1317-0507	3.391140	0.000000	12.74	1.75	12.58	0.05
104	Q1317-0507	3.391440	0.000000	10.22	0.94	12.80	0.04
105	Q1621-0042	3.391770	0.000000	13.10	0.59	13.26	0.02
106	Q1621-0042	3.392230	0.000010	10.18	0.49	13.44	0.02
107	Q1621-0042	3.392550	0.000000	11.79	0.35	13.61	0.01
108	Q1621-0042	3.474430	0.000000	16.10	3.71	12.75	0.18
109	Q1621-0042	3.474580	0.000060	11.93	5.15	12.86	0.45
110	Q1621-0042	3.474700	0.000000	13.43	3.75	12.75	0.41
111	Q1621-0042	3.488760	0.000010	15.43	1.15	13.13	0.03
112	Q1621-0042	3.489180	0.000010	11.03	2.06	12.87	0.08
113	Q1621-0042	3.489510	0.000030	9.50	2.71	12.57	0.11
114	Q1621-0042	3.498520	0.000010	19.27	1.55	12.76	0.03
115	Q1621-0042	3.501850	0.000020	28.86	2.45	12.79	0.03
116	Q1621-0042	3.546820	0.000010	14.34	0.00	12.54	0.02
117	Q1621-0042	3.547830	0.000000	6.86	1.00	12.49	0.05

118	Q1621-0042	3.548200	0.000000	11.07	2.47	12.96	0.23
119	Q1621-0042	3.548350	0.000000	16.88	3.73	13.29	0.18
120	Q1621-0042	3.548600	0.000000	6.81	1.67	12.77	0.22
121	Q1621-0042	3.548900	0.000000	17.54	0.86	13.48	0.02
122	Q1621-0042	3.549310	0.000000	5.65	0.20	13.34	0.01
123	Q1621-0042	3.550210	0.000000	22.31	2.29	12.96	0.03
124	Q1621-0042	3.550680	0.000000	19.77	1.01	13.28	0.02
125	Q1621-0042	3.551220	0.000000	8.47	1.10	12.70	0.05
126	Q1621-0042	3.551420	0.000000	2.44	0.00	12.22	0.08
127	Q1621-0042	3.551620	0.000000	14.06	1.89	12.84	0.05
128	Q1621-0042	3.621760	0.000010	10.41	1.01	12.73	0.03
129	Q1621-0042	3.622030	0.000010	5.15	1.42	12.23	0.09
130	Q1621-0042	3.651200	0.000020	17.77	2.07	12.71	0.04
131	Q1621-0042	3.669480	0.000000	13.95	0.00	12.42	0.00
132	Q1621-0042	3.673520	0.000010	16.79	1.07	13.35	0.03
133	Q1621-0042	3.674160	0.000010	21.00	1.26	13.61	0.02
134	Q1621-0042	3.674740	0.000000	12.25	0.33	13.68	0.01
135	Q1621-0042	3.675340	0.000000	13.82	0.17	14.03	0.01
136	Q1621-0042	3.676030	0.000000	13.21	0.39	13.32	0.01
137	Q1621-0042	3.746570	0.000010	9.57	1.15	12.63	0.04
138	Q1621-0042	3.764740	0.000030	22.78	3.08	12.54	0.04
139	Q1621-0042	3.765850	0.000220	40.47	13.92	12.91	0.20
140	Q1621-0042	3.766070	0.000010	10.53	0.00	12.86	0.06
141	Q1621-0042	3.766390	0.000010	11.01	0.00	12.72	0.10
142	Q1621-0042	3.766850	0.000020	21.23	0.00	13.07	0.05
143	Q1621-0042	3.767490	0.000010	10.34	0.72	12.79	0.02
144	Q1422+23	3.005960	0.000120	18.38	4.78	13.03	0.28
145	Q1422+23	3.006030	0.000020	6.20	4.32	12.31	0.72
146	Q1422+23	3.006290	0.000030	9.34	2.66	12.73	0.30
147	Q1422+23	3.006620	0.000020	13.82	1.61	12.63	0.04
148	Q1422+23	3.008530	0.000000	6.96	0.07	13.48	0.00
149	Q1422+23	3.023150	0.000010	12.63	1.16	12.15	0.03
150	Q1422+23	3.023550	0.000000	9.11	0.38	12.44	0.01
151	Q1422+23	3.081030	0.000010	8.76	0.84	11.98	0.03

152	Q1422+23	3.095440	0.000000	8.96	0.26	12.88	0.02
153	Q1422+23	3.095680	0.000010	11.82	1.09	12.50	0.05
154	Q1422+23	3.109660	0.000020	14.87	1.31	12.64	0.04
155	Q1422+23	3.109850	0.000010	4.23	1.67	11.92	0.21
156	Q1422+23	3.110010	0.000030	12.34	1.95	12.41	0.09
157	Q1422+23	3.234970	0.000010	5.57	1.00	12.02	0.09
158	Q1422+23	3.235240	0.000010	12.94	1.33	12.67	0.04
159	Q1422+23	3.235620	0.000010	12.52	0.75	12.68	0.03
160	Q0055-269	3.236210	0.000020	20.77	1.77	12.34	0.03
161	Q0055-269	3.241780	0.000010	14.57	1.19	12.16	0.03
162	Q0055-269	3.255750	0.000010	4.53	0.91	11.86	0.05
163	Q0055-269	3.256060	0.000000	11.96	0.29	12.85	0.01
164	Q0055-269	3.256580	0.000010	13.95	1.19	12.19	0.03
165	Q0055-269	3.260000	0.000010	7.84	0.95	11.90	0.04
166	J0124+0044	2.920170	0.000030	7.74	3.46	12.31	0.13
167	J0124+0044	2.976920	0.000010	8.35	0.65	12.65	0.03
168	J0124+0044	2.977430	0.000000	19.52	1.07	13.09	0.02
169	J0124+0044	2.977690	0.000000	8.09	0.26	13.16	0.01
170	J0124+0044	2.978220	0.000010	21.17	1.17	13.49	0.02
171	J0124+0044	2.978540	0.000000	8.58	0.68	12.97	0.06
172	J0124+0044	2.978810	0.000000	38.86	2.53	13.06	0.02
173	J0124+0044	3.002230	0.000010	11.08	1.31	12.37	0.04
174	J0124+0044	3.046020	0.000010	16.13	0.92	12.49	0.02
175	J0124+0044	3.046930	0.000010	19.80	0.89	12.71	0.02
176	J0124+0044	3.047010	0.000010	2.13	1.55	11.89	0.08
177	J0124+0044	3.172690	0.000020	27.81	1.68	12.96	0.02
178	J0124+0044	3.172790	0.000010	6.57	1.08	12.38	0.08
179	J0124+0044	3.179310	0.000030	27.48	3.69	12.51	0.05
180	J0124+0044	3.186870	0.000010	14.45	1.63	12.30	0.04
181	J0124+0044	3.190000	0.000120	11.90	5.48	12.66	0.39
182	J0124+0044	3.190110	0.000030	4.78	3.28	12.48	0.58
183	J0124+0044	3.190240	0.000020	5.94	1.42	12.81	0.14
184	J0124+0044	3.190570	0.000030	19.58	6.97	12.65	0.15
185	J0124+0044	3.191090	0.000010	17.86	1.07	13.20	0.03

186	J0124+0044	3.191610	0.000000	12.20	0.17	13.50	0.01
187	J0124+0044	3.192210	0.000010	22.92	0.57	13.23	0.01
188	J0124+0044	3.192450	0.000010	3.90	1.16	12.10	0.08
189	J0124+0044	3.228880	0.000020	16.67	1.68	12.38	0.04
190	J0124+0044	3.229770	0.000020	15.09	1.73	12.54	0.05
191	J0124+0044	3.230050	0.000020	4.87	3.02	11.76	0.25
192	J0124+0044	3.230000	0.000030	24.31	3.67	12.66	0.05
193	J0124+0044	3.250000	0.000010	14.77	0.56	12.78	0.01
194	J0124+0044	3.260060	0.000010	16.21	1.64	12.48	0.03
195	J0124+0044	3.322050	0.000020	20.28	1.82	12.72	0.03
196	J0124+0044	3.332150	0.000010	8.02	0.78	12.44	0.05
197	J0124+0044	3.332610	0.000030	33.32	2.06	13.28	0.03
198	J0124+0044	3.332980	0.000000	11.26	0.46	13.16	0.03
199	J0124+0044	3.333300	0.000000	7.58	0.46	12.73	0.03
200	J0124+0044	3.333750	0.000000	16.39	0.50	13.26	0.01
201	J0124+0044	3.334090	0.000010	6.01	1.06	12.19	0.08
202	J0124+0044	3.334340	0.000000	28.72	1.46	12.80	0.02
203	J0124+0044	3.336860	0.000010	12.40	1.09	12.68	0.03
204	J0124+0044	3.337360	0.000000	13.37	0.27	13.38	0.01
205	J0124+0044	3.389250	0.000000	7.28	0.33	12.65	0.01
206	J0124+0044	3.392290	0.000010	10.10	0.54	12.76	0.02
207	J0124+0044	3.392680	0.000020	12.31	1.83	12.34	0.05
208	J0124+0044	3.396580	0.000010	23.16	1.62	12.64	0.02
209	J0124+0044	3.445680	0.000020	16.06	2.14	12.96	0.04
210	J0124+0044	3.485630	0.000010	7.30	0.71	12.29	0.03
211	J0124+0044	3.505400	0.000000	14.79	0.40	12.99	0.01
212	J0124+0044	3.506000	0.000010	5.43	1.68	11.93	0.07
213	J0124+0044	3.508220	0.000010	15.13	1.35	12.55	0.03
214	J0124+0044	3.508710	0.000010	9.70	1.04	12.41	0.04
215	J0124+0044	3.509480	0.000010	7.60	1.27	12.13	0.05
216	J0124+0044	3.546750	0.000010	3.95	0.00	12.42	0.10
217	J0124+0044	3.546950	0.000020	10.85	0.00	12.83	0.04
218	J0124+0044	3.547800	0.000010	1.39	1.31	12.88	0.21
219	J0124+0044	3.547940	0.000000	14.90	0.32	13.91	0.01

220	J0124+0044	3.548830	0.000050	30.63	6.81	12.98	0.07
221	J0124+0044	3.549550	0.000010	10.22	0.86	13.42	0.05
222	J0124+0044	3.549940	0.000010	15.22	2.32	13.69	0.06
223	J0124+0044	3.550320	0.000040	11.21	3.55	12.99	0.23
224	J0124+0044	3.550000	0.000040	20.38	0.00	13.21	0.03
225	J0124+0044	3.551270	0.000020	14.78	2.91	12.88	0.08
226	J0124+0044	3.552030	0.000110	20.84	6.67	13.28	0.20
227	J0124+0044	3.552220	0.000010	4.18	2.38	12.59	0.23
228	J0124+0044	3.552440	0.000040	15.78	2.12	13.35	0.15
229	J0124+0044	3.556980	0.000000	7.33	0.42	12.83	0.03
230	J0124+0044	3.557380	0.000010	5.77	1.52	12.27	0.13
231	BRI1108-07	3.557690	0.000040	31.06	3.53	12.96	0.05
232	J0124+0044	3.562020	0.000050	25.31	2.57	12.73	0.06
233	J0124+0044	3.562330	0.000010	9.72	1.35	12.42	0.11
234	BRI1108-07	3.593400	0.000030	36.78	3.36	12.79	0.03
235	BRI1108-07	3.607020	0.000020	7.86	1.91	11.83	0.07
236	BRI1108-07	3.607400	0.000010	8.53	1.39	11.98	0.05
237	BRI1108-07	3.650740	0.000010	10.12	0.88	12.81	0.03
238	BRI1108-07	3.681330	0.000020	20.35	1.79	12.73	0.03
239	BRI1108-07	3.682000	0.000010	12.95	1.11	12.63	0.03
240	QB2000-330	2.920000	0.000010	19.88	0.96	13.05	0.04
241	QB2000-330	2.920260	0.000010	8.75	1.32	12.54	0.13
242	QB2000-330	2.956200	0.000010	12.69	0.94	12.39	0.02
243	QB2000-330	2.971080	0.000010	16.25	0.79	12.70	0.02
244	QB2000-330	2.971850	0.000010	19.25	0.62	13.18	0.02
245	QB2000-330	2.971940	0.000010	4.33	1.75	12.05	0.14
246	QB2000-330	2.972410	0.000040	19.51	3.88	12.39	0.08
247	QB2000-330	2.979430	0.000030	27.27	2.91	12.71	0.04
248	QB2000-330	2.979780	0.000010	7.99	1.56	12.19	0.11
249	QB2000-330	2.995920	0.000000	6.84	0.18	12.80	0.01
250	QB2000-330	2.998890	0.000040	19.84	4.12	12.23	0.08
251	QB2000-330	2.999360	0.000020	13.77	1.93	12.32	0.06
252	QB2000-330	3.020240	0.000010	10.34	0.81	12.42	0.04
253	QB2000-330	3.020610	0.000020	18.47	1.69	12.57	0.03

254	QB2000-330	3.058720	0.000010	12.54	0.56	12.99	0.02
255	QB2000-330	3.060210	0.000010	16.21	1.60	13.11	0.04
256	QB2000-330	3.060520	0.000020	8.15	2.72	12.51	0.18
257	QB2000-330	3.060790	0.000020	9.64	1.92	12.61	0.08
258	QB2000-330	3.061100	0.000000	12.36	3.33	12.32	0.09
259	PKS1937-101	3.065470	0.000030	33.27	2.32	13.58	0.05
260	PKS1937-101	3.066090	0.000010	8.37	1.17	12.78	0.06
261	PKS1937-101	3.066990	0.000020	10.75	2.72	12.38	0.10
262	PKS1937-101	3.067500	0.000020	9.41	2.48	12.40	0.09
263	PKS1937-101	3.068100	0.000050	18.69	6.74	12.41	0.12
264	PKS1937-101	3.105150	0.000080	12.13	3.13	12.82	0.32
265	PKS1937-101	3.105380	0.000020	11.47	4.35	13.14	0.29
266	PKS1937-101	3.105710	0.000030	13.38	4.99	13.51	0.19
267	PKS1937-101	3.105930	0.000010	7.54	1.74	13.50	0.22
268	PKS1937-101	3.106110	0.000010	8.14	1.75	13.68	0.13
269	PKS1937-101	3.106320	0.000030	9.49	2.41	13.34	0.23
270	PKS1937-101	3.106580	0.000030	23.49	2.65	13.73	0.06
271	PKS1937-101	3.107130	0.000000	11.58	0.63	13.19	0.03
272	PKS1937-101	3.107460	0.000000	9.61	0.52	12.94	0.02
273	PKS1937-101	3.107850	0.000000	11.54	0.21	13.23	0.01
274	PKS1937-101	3.108410	0.000000	9.85	0.21	13.60	0.01
275	PKS1937-101	3.108650	0.000010	6.73	0.73	13.54	0.06
276	PKS1937-101	3.108820	0.000020	6.25	2.45	13.41	0.43
277	PKS1937-101	3.108970	0.000050	8.63	4.33	13.53	0.33
278	PKS1937-101	3.109260	0.000010	9.23	0.93	14.01	0.05
279	PKS1937-101	3.109450	0.000020	8.42	0.69	13.45	0.13
280	PKS1937-101	3.152190	0.000010	18.15	1.42	12.29	0.03
281	J0124+0044	3.200030	0.000010	17.36	0.68	12.87	0.01
282	J0124+0044	3.200950	0.000030	28.49	2.17	12.88	0.04
283	J0124+0044	3.201260	0.000000	7.76	0.59	12.70	0.04
284	J0124+0044	3.212430	0.000020	14.61	1.66	12.53	0.04
285	J0124+0044	3.212700	0.000010	6.34	1.60	12.17	0.15
286	J0124+0044	3.212960	0.000030	15.73	3.01	12.40	0.08
287	J0124+0044	3.241100	0.000010	6.05	1.33	12.10	0.13

288	J0124+0044	3.241140	0.000010	19.36	2.12	12.50	0.05
289	J0124+0044	3.304670	0.000000	5.61	0.55	12.18	0.02
290	J0124+0044	3.486830	0.000090	18.08	6.25	12.74	0.18
291	J0124+0044	3.487050	0.000020	5.22	3.76	12.22	0.41
292	J0124+0044	3.487370	0.000010	10.64	1.33	13.07	0.05
293	J0124+0044	3.487680	0.000020	8.30	1.98	12.54	0.11
294	J0124+0044	3.489770	0.000020	9.84	2.05	12.36	0.07
295	J0124+0044	3.543860	0.000020	16.73	2.37	12.52	0.05
296	J0124+0044	3.556430	0.000040	12.95	2.78	12.60	0.11
297	J0124+0044	3.556710	0.000020	8.83	1.51	12.50	0.12
298	J0124+0044	3.614210	0.000010	9.88	0.70	12.40	0.02
299	BRI1108-07	2.900000	0.000010	0.87	7.10	11.58	0.16
300	BRI1108-07	2.900630	0.000010	19.08	0.60	13.04	0.01
301	BRI1108-07	2.922520	0.000010	2.91	1.03	11.93	0.04
302	BRI1108-07	2.922910	0.000000	10.95	0.56	12.54	0.02
303	BRI1108-07	2.933140	0.000000	6.29	1.69	12.36	0.09
304	BRI1108-07	2.933370	0.000020	13.64	0.00	12.65	0.04
305	BRI1108-07	2.934170	0.000010	9.70	0.00	12.69	0.03
306	BRI1108-07	3.070720	0.000010	8.50	1.17	12.54	0.06
307	BRI1108-07	3.070910	0.000000	22.23	4.01	12.80	0.06
308	BRI1108-07	3.091800	0.000060	28.03	4.60	12.53	0.08
309	BRI1108-07	3.092120	0.000000	9.55	0.38	12.91	0.03
310	BRI1108-07	3.178360	0.000010	10.08	0.00	12.46	0.02
311	BRI1108-07	3.276870	0.000000	14.47	0.50	12.67	0.01
312	BRI1108-07	3.277370	0.000000	11.24	0.22	12.89	0.01
313	BRI1108-07	3.286260	0.000010	8.05	1.48	12.31	0.08
314	BRI1108-07	3.286500	0.000020	37.05	2.06	13.15	0.02
315	BRI1108-07	3.287160	0.000010	8.42	1.28	12.54	0.10
316	BRI1108-07	3.287500	0.000010	16.57	1.07	13.21	0.02
317	BRI1108-07	3.288010	0.000000	9.83	0.16	13.75	0.01
318	BRI1108-07	3.288400	0.000000	12.44	0.41	13.69	0.01
319	BRI1108-07	3.288760	0.000010	13.51	0.49	13.40	0.02
320	BRI1108-07	3.293970	0.000020	25.13	2.17	12.68	0.03
321	BRI1108-07	3.302000	0.000000	23.22	0.00	12.50	0.14

322	BRI1108-07	3.302140	0.000000	13.64	2.77	12.58	0.17
323	BRI1108-07	3.302410	0.000020	16.88	1.73	12.92	0.05
324	BRI1108-07	3.303310	0.000030	27.96	3.47	12.61	0.04
325	BRI1108-07	3.320420	0.000050	7.67	6.40	11.82	0.30
326	BRI1108-07	3.320690	0.000020	8.40	3.59	12.17	0.15
327	BRI1108-07	3.320950	0.000010	5.87	1.55	12.08	0.08
328	BRI1108-07	3.359410	0.000000	6.42	0.31	12.58	0.01
329	BRI1108-07	3.359850	0.000000	9.57	0.89	12.48	0.04
330	BRI1108-07	3.360020	0.000010	9.05	0.72	12.64	0.03
331	BRI1108-07	3.371770	0.000060	25.99	3.45	12.54	0.09
332	BRI1108-07	3.371970	0.000010	9.17	0.69	12.77	0.05
333	BRI1108-07	3.377030	0.000000	17.88	7.00	12.63	0.61
334	BRI1108-07	3.377080	0.000020	13.22	1.62	13.06	0.25
335	BRI1108-07	3.377440	0.000040	9.45	3.07	12.02	0.21
336	BRI1108-07	3.411430	0.000010	7.94	1.09	12.26	0.04
337	BRI1108-07	3.446440	0.000060	13.57	3.53	12.78	0.26
338	BRI1108-07	3.446720	0.000060	14.17	2.28	12.91	0.17
339	BRI1108-07	3.571090	0.000120	13.31	5.33	12.84	0.31
340	BRI1108-07	3.571250	0.000010	6.13	2.45	12.63	0.44
341	BRI1108-07	3.571560	0.000040	8.75	4.93	12.27	0.22
342	BRI1108-07	3.571790	0.000030	5.12	3.16	11.95	0.25
343	BRI1108-07	3.574400	0.000000	32.53	19.59	12.43	0.19
344	BRI1108-07	3.574700	0.000000	10.42	4.18	12.37	0.58
345	BRI1108-07	3.575040	0.000150	21.27	12.73	13.20	0.57
346	BRI1108-07	3.575570	0.000280	25.64	23.14	13.19	0.58
347	BRI1108-07	3.576220	0.000080	16.29	5.25	12.73	0.28
348	BRI1108-07	3.581280	0.000010	6.38	1.51	12.31	0.14
349	BRI1108-07	3.581600	0.000000	7.01	0.84	12.56	0.09
350	BRI1108-07	3.582030	0.000070	37.02	12.08	13.03	0.13
351	Q0055-269	2.913890	0.000010	20.00	1.09	12.78	0.02
352	Q0055-269	2.945270	0.000010	18.43	0.58	12.94	0.01
353	Q0055-269	2.949010	0.000030	22.04	2.13	12.94	0.05
354	Q0055-269	2.949210	0.000010	4.12	1.25	12.21	0.11
355	Q0055-269	2.949530	0.000020	15.06	1.68	12.62	0.06

356	Q0055-269	2.950130	0.000010	17.13	1.15	12.77	0.02
357	Q0055-269	2.950000	0.000000	6.36	0.58	12.60	0.03
358	Q0055-269	2.950740	0.000000	21.31	0.37	13.53	0.01
359	Q0055-269	2.951410	0.000000	18.16	0.55	13.07	0.01
360	Q0055-269	2.951930	0.000000	8.37	0.49	12.51	0.02
361	Q0055-269	3.004810	0.000020	7.98	1.86	12.14	0.12
362	Q0055-269	3.005040	0.000010	9.85	1.07	12.54	0.05
363	Q0055-269	3.038770	0.000010	11.22	0.00	12.56	0.02
364	Q0055-269	3.038930	0.000000	12.95	2.65	12.23	0.07
365	Q0055-269	3.083800	0.000010	7.66	1.34	12.10	0.05
366	Q0055-269	3.085280	0.000000	7.50	0.00	11.94	0.07
367	Q0055-269	3.085710	0.000000	14.69	1.43	12.59	0.03
368	Q0055-269	3.085900	0.000000	7.26	0.34	12.98	0.01
369	Q0055-269	3.086160	0.000010	8.45	1.51	12.30	0.06
370	Q0055-269	3.132320	0.000010	10.08	1.84	12.27	0.05
371	Q0055-269	3.132620	0.000010	10.08	1.84	12.27	0.05
372	Q0055-269	3.179170	0.000010	4.24	1.00	12.33	0.04
373	Q0055-269	3.190190	0.000000	12.66	9.42	12.83	0.27
374	Q0055-269	3.190440	0.000010	9.07	0.99	13.88	0.05
375	Q0055-269	3.190950	0.000030	8.05	1.96	13.87	0.12
376	Q0055-269	3.191180	0.000040	7.31	3.97	13.59	0.22
377	Q0055-269	3.191540	0.000030	13.24	4.54	13.73	0.11
378	Q0055-269	3.191810	0.000000	6.80	3.07	13.36	0.20
379	Q0055-269	3.192070	0.000000	15.00	0.00	13.71	0.05
380	Q0055-269	3.192800	0.000000	25.78	0.00	12.70	0.00
381	Q0055-269	3.194180	0.000000	5.68	0.24	13.17	0.02
382	Q0055-269	3.194280	0.000020	35.74	1.29	13.43	0.02
383	Q0055-269	3.194470	0.000000	13.07	0.58	13.30	0.03
384	Q0055-269	3.195020	0.000010	4.45	1.47	12.05	0.09
385	Q0055-269	3.248120	0.000000	4.57	0.59	12.50	0.03
386	Q0055-269	3.248450	0.000010	9.91	1.28	12.51	0.04
387	Q0055-269	3.255940	0.000010	10.83	1.21	12.87	0.05
388	Q0055-269	3.256210	0.000010	9.72	0.70	13.08	0.04
389	Q0055-269	3.256640	0.000020	12.01	2.07	12.74	0.08

390	Q0055-269	3.256950	0.000010	10.14	1.14	12.86	0.06
391	Q0055-269	3.257370	0.000010	16.09	0.88	12.95	0.02
392	Q0055-269	3.258330	0.000030	10.15	4.63	12.23	0.13
393	Q0055-269	3.423390	0.000010	13.37	1.42	12.50	0.04
394	Q0055-269	3.423970	0.000000	19.48	2.88	12.46	0.05
395	Q0055-269	3.526270	0.000000	30.53	0.00	12.83	0.02
396	Q0055-269	3.527110	0.000000	16.05	0.44	13.22	0.01
397	Q0055-269	3.527670	0.000020	15.77	1.65	12.63	0.04
398	Q0055-269	3.528430	0.000020	17.78	2.21	12.44	0.04
399	Q0055-269	3.555380	0.000010	7.78	0.51	12.88	0.03
400	Q0055-269	3.555660	0.000010	10.35	0.64	13.02	0.02
401	Q0055-269	3.556080	0.000000	24.40	0.90	13.09	0.01
402	Q0055-269	3.557050	0.000010	11.96	0.92	12.52	0.03
403	Q0055-269	3.558260	0.000010	13.23	0.97	12.55	0.03
404	Q0055-269	3.573230	0.000060	89.67	11.18	13.49	0.05
405	Q0055-269	3.585270	0.000010	21.01	0.88	12.75	0.02
406	Q0055-269	3.591010	0.000000	8.92	0.41	12.61	0.01
407	Q0055-269	3.599860	0.000010	11.01	0.94	12.63	0.03
408	Q1317-0507	3.600470	0.000010	10.35	0.47	13.11	0.02
409	Q1317-0507	3.600870	0.000000	11.11	0.44	13.31	0.01
410	Q1317-0507	3.601460	0.000000	16.49	0.38	13.73	0.01
411	Q1317-0507	3.601880	0.000010	9.36	0.49	13.07	0.03
412	Q1317-0507	3.603180	0.000010	11.39	0.45	13.42	0.04
413	Q1317-0507	3.603500	0.000020	15.18	1.30	13.24	0.05
414	Q1621-0042	2.909660	0.000000	8.90	0.43	12.46	0.01
415	Q1621-0042	2.910040	0.000010	10.91	1.95	11.95	0.05
416	Q1621-0042	2.947220	0.000010	6.56	1.96	11.45	0.08
417	Q1621-0042	2.947510	0.000000	7.73	0.21	12.48	0.01
418	Q1621-0042	2.960620	0.000010	14.63	0.98	12.55	0.02
419	Q1621-0042	2.961080	0.000010	13.72	0.87	12.70	0.02
420	Q1621-0042	2.961440	0.000000	8.10	0.41	12.63	0.02
421	Q1621-0042	2.961950	0.000000	19.19	0.49	13.28	0.01
422	Q1621-0042	2.962330	0.000000	11.04	0.42	12.84	0.02
423	Q1621-0042	2.971360	0.000020	20.11	1.69	12.60	0.04

424	Q1621-0042	2.971630	0.000020	6.55	4.99	11.43	0.44
425	Q1621-0042	2.975180	0.000010	7.02	1.51	11.66	0.06
426	Q1621-0042	2.975800	0.000030	24.07	2.84	12.39	0.05
427	Q1621-0042	2.976200	0.000000	10.26	0.24	12.81	0.01
428	Q1621-0042	2.999200	0.000010	18.78	0.56	12.71	0.01
429	Q1621-0042	3.035020	0.000000	8.30	0.48	12.12	0.02
430	Q1621-0042	3.036580	0.000010	15.22	1.52	12.18	0.04
431	Q1621-0042	3.036910	0.000010	8.18	1.65	11.78	0.08
432	Q1621-0042	3.063370	0.000010	26.23	1.01	12.98	0.01
433	Q1621-0042	3.064320	0.000010	12.28	0.73	12.65	0.02
434	QB2000-330	3.069580	0.000020	9.26	1.78	12.09	0.06
435	QB2000-330	3.070160	0.000010	2.83	1.83	11.73	0.08
436	QB2000-330	3.071000	0.000000	5.29	0.59	12.24	0.03
437	QB2000-330	3.089860	0.000010	13.34	0.76	12.94	0.04
438	QB2000-330	3.090170	0.000020	20.03	0.00	13.17	0.02
439	QB2000-330	3.090530	0.000000	20.17	0.00	12.99	0.02
440	QB2000-330	3.091050	0.000000	10.67	0.28	13.01	0.01
441	QB2000-330	3.094660	0.000010	17.26	1.13	12.23	0.02
442	QB2000-330	3.119290	0.000020	13.30	2.20	11.91	0.06
443	QB2000-330	3.119690	0.000010	12.00	1.38	12.05	0.04
444	QB2000-330	3.132510	0.000020	30.83	1.84	12.57	0.02
445	QB2000-330	3.133770	0.000010	17.77	0.88	12.81	0.02
446	QB2000-330	3.134080	0.000010	5.62	0.89	12.18	0.07
447	QB2000-330	3.134450	0.000000	16.47	0.38	13.00	0.01
448	QB2000-330	3.137090	0.000010	13.02	1.35	12.61	0.12
449	QB2000-330	3.137140	0.000030	29.05	5.26	12.61	0.10
450	QB2000-330	3.138070	0.000020	20.63	2.20	12.27	0.04
451	QB2000-330	3.191400	0.000000	8.51	0.48	12.13	0.02
452	QB2000-330	3.233290	0.000010	8.30	1.29	12.03	0.05
453	QB2000-330	3.242570	0.000010	3.67	1.07	11.53	0.05
454	QB2000-330	3.256780	0.000020	14.59	2.40	12.05	0.07
455	QB2000-330	3.257350	0.000020	22.38	3.34	12.30	0.05
456	QB2000-330	3.265400	0.000020	9.95	1.78	12.06	0.11
457	QB2000-330	3.265740	0.000020	17.68	1.43	12.60	0.03

458	QB2000-330	3.275940	0.000010	11.47	0.96	11.89	0.03
459	QB2000-330	3.317960	0.000010	13.79	1.04	12.19	0.03
460	QB2000-330	3.379930	0.000010	15.30	1.11	12.57	0.02
461	QB2000-330	3.380420	0.000010	11.91	1.17	12.37	0.03
462	QB2000-330	3.381340	0.000000	7.43	1.38	12.03	0.07
463	QB2000-330	3.381640	0.000000	11.62	0.17	13.28	0.00
464	QB2000-330	3.382200	0.000000	14.00	0.22	13.24	0.01
465	QB2000-330	3.382680	0.000000	8.59	0.50	12.62	0.02
466	QB2000-330	3.383170	0.000040	21.22	4.82	12.16	0.08
467	QB2000-330	3.410790	0.000010	12.72	1.27	12.25	0.03
468	QB2000-330	3.411450	0.000010	17.96	0.52	12.80	0.01
469	QB2000-330	3.446900	0.000010	9.69	0.56	13.01	0.02
470	QB2000-330	3.447350	0.000000	12.36	0.33	13.41	0.01
471	QB2000-330	3.470020	0.000000	5.06	0.38	12.52	0.02
472	QB2000-330	3.471140	0.000010	3.33	1.70	11.84	0.08
473	QB2000-330	3.476150	0.000020	8.08	2.12	12.08	0.08
474	QB2000-330	3.479390	0.000030	13.93	2.42	12.46	0.09
475	QB2000-330	3.479800	0.000040	14.62	3.10	12.40	0.10
476	QB2000-330	3.48000	0.000010	13.49	1.25	12.42	0.03
477	QB2000-330	3.494850	0.000010	9.96	0.62	12.42	0.02
478	QB2000-330	3.514620	0.000000	7.95	0.29	12.83	0.02
479	QB2000-330	3.514950	0.000010	13.45	1.35	12.51	0.04
480	QB2000-330	3.534980	0.000000	18.52	0.00	12.88	0.02
481	QB2000-330	3.535970	0.000010	23.19	0.47	13.73	0.01
482	QB2000-330	3.536660	0.000020	22.06	2.33	13.05	0.05
483	QB2000-330	3.537350	0.000000	19.09	0.47	13.24	0.01
484	QB2000-330	3.538460	0.000000	26.34	4.96	13.35	0.14
485	QB2000-330	3.538700	0.000000	9.56	0.62	13.58	0.06
486	QB2000-330	3.539310	0.000020	12.18	3.88	13.36	0.72
487	QB2000-330	3.539430	0.000320	17.25	6.56	13.23	1.02
488	QB2000-330	3.539950	0.000080	37.91	5.22	12.94	0.07